





## Long-range hydrogen-binding effects of carbide interfaces in iron

Xiaochuan Tang \* and Rofiques Salehin 


*Department of Mechanical Engineering, Colorado State University, Fort Collins, Colorado 80523, USA*

Gregory B. Thompson 

*The University of Alabama, Department of Metallurgical and Materials Engineering, 401, 7th Avenue,  
285 Hardaway Hall, Tuscaloosa, Alabama 35487, USA*

Christopher R. Weinberger 

*Department of Mechanical Engineering, Colorado State University, Fort Collins, Colorado 80523, USA  
and School of Advanced Materials Discovery, Colorado State University, Fort Collins, Colorado 80523, USA*

 (Received 12 May 2021; revised 13 August 2021; accepted 29 September 2021; published 14 October 2021)

A micromechanics model was developed to evaluate the elastic binding energy between carbide precipitates and hydrogen interstitials using Eshelby's equivalent inclusion method. Density functional theory (DFT) simulations were performed to obtain the material-specific quantities, e.g., lattice constants and the elastic constants, for the continuum model. Using this model, we find that for coherent carbide precipitates, hydrogen atoms are more likely to bind on the broad surfaces of the disk-like precipitates, which is consistent with experimental observations. For semicoherent and incoherent precipitates, our model suggests that it is possible for semicoherent precipitates to have significant hydrogen binding capability while there is no hydrogen-binding capability of incoherent precipitates, which also agrees with experimental findings. In addition, several factors that influence the binding energies between hydrogen atoms and carbide precipitates were quantitatively analyzed, including the precipitate size, morphology, orientation, and interface. These collective results include both the position and the value of the strongest hydrogen-binding interaction for a wide range of carbide stoichiometries, which contributes to our understanding of hydrogen trapping in steel-based materials.

DOI: [10.1103/PhysRevMaterials.5.103603](https://doi.org/10.1103/PhysRevMaterials.5.103603)

### I. INTRODUCTION

High strength steels are susceptible to hydrogen embrittlement (HE) and specifically hydrogen-induced delayed fracture (HDF). Microalloying with transition metals has been shown to improve high strength steels resistance to HDF [1–4], and the main proposed reason for this improvement is the presence of small scale carbide precipitates. Specifically, the precipitation of titanium carbides (TiC), vanadium carbide (VC), niobium carbides (NbC), and molybdenum carbides (Mo<sub>2</sub>C) are thought to positively impact the materials resistance to HDF.

These (mostly) rocksalt phases (B1 structure) form following a standard precipitate growth pattern in which the smallest particles are coherent with the ferrite matrix, exhibiting the Baker-Nutting relation [5,6], as platelets. As the precipitates grow, they transition to semicoherent precipitates with misfit dislocations and eventually to incoherent precipitates [7]. During this growth, the particles undergo a constant change in shape, transitioning from platelets (coherent) to spherical particles (incoherent). The report of TiC particles acting as traps to hydrogen is well known [1,8–15], with these traps originally reported to be strong traps [1,9,10]. This leads to

many studies to determine where and how the hydrogen was trapped [12–15]. Several studies have demonstrated that coherency plays an important role in determining the mechanics of trapping. Notably, coherent and semicoherent TiC particles trap hydrogen at the interface with trapping sites presumed to occur at dislocation cores with hydrogen desorption values of 40–60 kJ/mol [14,15]. Furthermore, the desorption activation energies for incoherent particles are reported to be higher, with values ranging from 70 to 120 kJ/mol [14]. Finally, Takahashi *et al.* has directly demonstrated trapping in coherent platelets [16] by means of the atom probe tomography (APT).

NbC and VC particles have also been studied as potential hydrogen traps in steels. However, there is a lack of consensus about if and where NbC and VC trap hydrogen. For example, in vanadium carbides, the study by Wei *et al.* concluded that hydrogen was trapped at the interface of coherent and semicoherent particles [7]. In contrast, Takahashi *et al.* [17,18] and Chen *et al.* [19] both demonstrated that hydrogen can be stored inside the VC particles and concluded they were not stored at the interface. In niobium carbides, Chen *et al.* directly observed hydrogen at the interface and the interior of incoherent NbC particles [20]. Similarly, Ohnuma *et al.* concluded that trapping could occur at the interface and within bulk using small angle neutron scattering, with these particles presumably coherent and semicoherent based on their sizes [21]. Wei *et al.* further suggested that hydrogen was trapped

\*Corresponding author: [xtang@ucdavis.edu](mailto:xtang@ucdavis.edu)

at the interface of coherent and semicoherent NbC particles, while the incoherent NbC particles did not exhibit the hydrogen trapping [7].

For the carbide precipitates without a FCC metal sublattice, Wei and Tsuzaki [22] compared the hydrogen trapping of the molybdenum hemicarbide ( $\text{Mo}_2\text{C}$ ) with some B1-structure carbides (TiC, VC, NbC) in four steels and concluded that  $\text{Mo}_2\text{C}$  was not as a promising hydrogen trap as other B1-structure carbides. However, Lee *et al.* [23] reported that  $\text{MoC}_x$  exhibited good hydrogen embrittlement (HE) resistance, which was also found by Depover *et al.* [4]. Thus, there is a lack of consensus of the role of interface and bulk trapping of transition metal carbides in steels. It may occur at the interfaces or in the bulk, and the evidence seems not to produce a conclusion regarding the role of coherency.

In order to better understand the roles that different mechanisms can play in trapping hydrogen, it is critical to evaluate each mechanism in its own right. To this end, in this theoretical paper we examine the potential trapping energy of hydrogen at the interfaces of carbide particles in steels. More specifically, we examine the elastic interactions between coherent carbide particles and H atoms inside the host iron matrix using the formalisms of the Eshelby equivalent inclusion [24,25]. These results not only suggest where the attractive binding energies occur, which is on the broad surface of the coherent carbide particles, but they also establish the magnitude of such interactions. Furthermore, several factors of this long-range hydrogen-binding energy are analyzed, such as precipitate sizes, morphologies, and interface characters. At last, comparisons of this attractive hydrogen interaction are carried out among the group IVB, VB, and VIB carbides with different stoichiometries. The magnitude of the long-range hydrogen binding increases as the coherent carbide precipitate grows. However, this binding energy becomes negligible when the carbide particle grows sufficiently and becomes an incoherent precipitate. For coherent carbide precipitates, the magnitude of the hydrogen-binding energy depends both on the elasticity and the lattice constant of carbides. For carbides with a face-centered-cubic (FCC) metal sublattice, also known as the B1-structure based carbides, zirconium carbide (ZrC) exhibits the largest attractive hydrogen interaction at its interface. For carbides with a hexagonal metal sublattice, the group VB and VIB hemicarbides show promising hydrogen-binding capabilities. Therefore, results in the present paper not only assist in understanding long-range interactions between carbide particles and hydrogen, but also provide insights into the material selection of HE resistance steels.

## II. METHODOLOGY

### A. Model development

When steels are exposed in the hydrogen environment, atomic hydrogen (H) dissolves in iron and diffuses into its interior via interstitial diffusion. After sufficient time, H will diffuse to the grain boundaries, dislocations, and other defects, which reduces the ductility and strength of steels, resulting in hydrogen embrittlement [26,27]. A schematic illustrating H diffusion in steels is shown in Fig. 1(a) where both H atoms

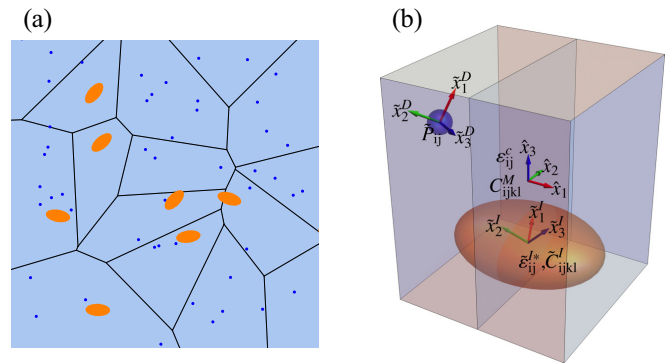


FIG. 1. (a) A schematic of absorbed H in steels. The blue dots represent H atoms and the orange ellipses represent the carbide particles. (b) A schematic illustrating our simplified model: The blue sphere represents the point defect (a H atom) and the orange ellipsoid represents the inclusion (a carbide particle). The global coordinates  $\hat{x}_i$  are set along the semiaxes of the ellipsoidal inclusion. The local coordinates  $\hat{x}_i^D$  and  $\hat{x}_i^I$  represent the orientation of the point defect and the inclusion, respectively.

and carbide particles can be considered as inhomogeneities inside the matrix (steel). These inhomogeneities create internal sources of displacements, strains and stresses [28], which results in the elastic interaction between defects. If the total elastic energy decreases as the hydrogen approaches the carbide interface, then the carbide acts as a trap for hydrogen. This energy change is termed the interaction energy in elasticity theory  $E_{\text{int}}$  and is equivalent to the trap energy discussed in the hydrogen community. A negative value of  $E_{\text{int}}$  indicates the ability of the carbide particles elastic field to trap hydrogen and its magnitude representing the strength of the trap. To evaluate  $E_{\text{int}}$ , we propose a simplified two-body continuum model including a single H atom and a single carbide particle inside an infinite matrix as shown in Fig. 1(b). The matrix in this model is iron (Fe), which we approximate as an isotropic continuum with the elastic constants  $C_{ijkl}^{M-\text{iso}}$ :

$$C_{ijkl}^{M-\text{iso}} = G \left( \frac{2\nu}{1-2\nu} \delta_{ij} \delta_{kl} + \delta_{ik} \delta_{jl} + \delta_{jk} \delta_{il} \right), \quad (1)$$

where  $\delta_{ij}$  is the Kronecker delta,  $G$  is the shear modulus,  $\nu$  is Poisson's ratio, and the Young's modulus is  $E = 2G(1 + \nu)$ . The H atom is modeled as a point defect with an elastic dipole tensor  $\tilde{P}_{ij}$ , which is defined in its local coordinates  $\hat{x}_i^D$  [29]. We are aware that the choice of the anisotropic iron matrix would be more appropriate. However, the choice of an isotropic matrix leads to a closed-form solution, which not only significantly lowers the computational complexity, but more importantly assists in our analyses of the underlying factors that affect the long-range hydrogen-binding effect, such as the shape, size, structure and elastic constants of the carbides, as well as the lattice and elastic constants of the iron matrix. The carbide particle is modeled as an ellipsoidal inclusion with semiaxes  $(a_1, a_2, a_3)$  with its own elastic stiffness tensor  $\tilde{C}_{ijkl}^{I*}$  expressed in its own coordinate system  $\hat{x}_i^I$ . If the inclusion remains at least partially coherent with the matrix, the inclusion will develop an eigenstrain  $\tilde{\epsilon}_{ij}^{I*}$ , which results in a constraint strain  $\epsilon_{ij}^c$  in the matrix. It is this constraint strain

that elastically interacts with the elastic fields of the H atom in the matrix, which leads to the interaction energy  $E_{\text{int}}$ . To derive the explicit form of  $E_{\text{int}}$ , we set the global coordinates  $\hat{x}_i$  along the semiaxes of the ellipsoidal inclusion, while the local coordinates,  $\tilde{x}_i^D$  and  $\tilde{x}_i^I$  (which represent the orientation of the point defect and the inclusion, respectively) are chosen to easily represent  $\tilde{P}_{ij}$  and  $\tilde{C}_{ijkl}^*$ . The orientation of the local coordinates  $\tilde{x}_i^D$  and  $\tilde{x}_i^I$  are known based on crystallography. With the use of the rotation matrix  $R$ , the known physical quantities in local coordinates can be transformed to those in global coordinates:

$$\hat{x}_i = R_{ij}^D \tilde{x}_j^D, \quad \hat{x}_i = R_{ij}^I \tilde{x}_j^I, \quad (2)$$

$$P_{ij} = R_{im}^D R_{jn}^D \tilde{P}_{mn}, \quad \varepsilon_{ij}^{I*} = R_{im}^I R_{jn}^I \tilde{\varepsilon}_{mn}^{I*}, \quad (3)$$

$$C_{ijkl}^I = R_{im}^I R_{jn}^I R_{kp}^I R_{lq}^I \tilde{C}_{mnpq}^I, \quad (4)$$

where the variables with tilde stand for physical quantities in the local coordinates while those without tilde stand for physical quantities in the global coordinates. In the following context, the derivations and computations are carried out in the global coordinates  $\hat{x}_i$ . For an ellipsoidal inclusion inside an infinite matrix, Eshelby derived the analytical solution, where the constraint strain  $\varepsilon_{ij}^c$  is expressed as the tensor product of the eigenstrain  $\varepsilon_{ij}^*$  and the Eshelby tensor  $D_{ijkl}$  [24,25]:

$$\varepsilon_{ij}^c(\text{in}) = D_{ijkl}^{\text{in}} \varepsilon_{kl}^*, \quad \varepsilon_{ij}^c(\text{out}) = D_{ijkl}^{\text{out}} \varepsilon_{kl}^*, \quad (5)$$

In Eq. (5),  $D_{ijkl}^{\text{in}}$  and  $D_{ijkl}^{\text{out}}$  represents the Eshelby tensor inside and outside the inclusion, respectively. We note that Eq. (5) is for a homogeneous ellipsoidal inclusion where the elasticity of the inclusion is the same with that of the matrix. To deal with the ellipsoidal inhomogeneity in our model, the Eshelby equivalent inclusion method is used and the equivalent eigenstrain  $\varepsilon_{ij}^*$  is computed as

$$[(C_{ijkl}^I - C_{ijkl}^{M-\text{iso}})D_{klmn}^{\text{in}} + C_{ijmn}^{M-\text{iso}}] \varepsilon_{mn}^* = C_{ijkl}^I \varepsilon_{kl}^{I*}. \quad (6)$$

And the elastic-strain interaction energy  $E_{\text{int}}$  is evaluated subsequently as

$$E_{\text{int}} = -P_{ij} \varepsilon_{ij}^c. \quad (7)$$

In this model, the Eshelby tensor for an ellipsoidal inclusion has an analytic form, which dramatically simplifies the solution for the interaction energy. Inside an ellipsoidal inclusion, the Eshelby tensor  $D_{ijkl}^{\text{in}}$  is a constant and only depends on the inclusion shape (the ratios of the semiaxes  $a_i$ ) [30]. At a point  $x_i$  outside an ellipsoidal inclusion, the Eshelby tensor  $D_{ijkl}^{\text{out}}$  has a simple explicit expression in terms of the inclusion shape ( $a_i$ ) and the point coordinates ( $x_i$ ) [31]. Corresponding derivations are covered in the Supplemental Material [32]. The unknown terms in this model are material-specific quantities, including the elastic stiffness tensor of iron  $C_{ijkl}^{M-\text{iso}}$ , the eigenstrain  $\tilde{\varepsilon}_{ij}^{I*}$ , the elastic constants of the carbides  $\tilde{C}_{ijkl}^{I*}$ , and the elastic dipole tensor  $\tilde{P}_{ij}$  of a H atom. For the matrix, the crystal structure and elastic constants of  $\alpha$ -Fe and  $\gamma$ -Fe are obtained from reported experimental values. For the inclusion, we investigated the group IVB, VB, and VIB carbides  $\text{MC}_x$  with  $x$  from 0.5 to 1, which include both experimentally reported structures and vacancy-ordered structures predicted by

density functional theory (DFT) [33]. To ensure consistency of the lattice constants and elastic constants of the various carbides, these values were determined via DFT calculations in this paper. The elastic dipole tensor of a H atom was extracted from DFT calculations using the homogeneous stress method [29] because of the lack of direct experimental measurements of the dilation of the iron/steel matrix caused by H atoms. The determination of the aforementioned unknown terms is covered with details in the proceeding sections. In addition, we are aware that in this model the matrix is pure Fe, which differs from ferritic/austenitic/martensitic steels. However, starting with the pure Fe matrix will provide a clear relationship between the interaction energy  $E_{\text{int}}$  and the material-specific properties of the matrix, which paves ways for evaluating the interaction energy between H and carbide particles inside steels with more complex chemistries.

## B. The structure and elasticity of the matrix and inclusion

The two allotropes of iron,  $\alpha$ -Fe and  $\gamma$ -Fe, are chosen as the isotropic matrix in this model, which is required by the closed-form Eshelby's solution.  $\alpha$ -Fe is ferromagnetic and has the body-centered cubic (BCC) structure, which is essentially the matrix of ferritic steels.  $\gamma$ -Fe is paramagnetic and has the face-centered cubic (FCC) structure, which is similar to austenitic steels. For iron and steels, a number of studies have investigated the structure and elastic constants via both computational and experimental approaches [34–40]. To make the matrix as representative as ferrite as possible, we use the reported experimental values of the lattice parameter and elastic constants of  $\alpha$ -Fe in our calculation [34,35], which are listed in Table I. Likewise, the experimental values are used for  $\gamma$ -Fe as well [34,36]. The anisotropic elastic constants of both  $\alpha$ -Fe and  $\gamma$ -Fe ( $C_{11}$ ,  $C_{12}$ ,  $C_{44}$ ) were determined experimentally by means of neutron scattering measurements and ultrasonic pulse-echo measurements [36–38]. The isotropic elastic constants of Fe were computed from the anisotropic elastic constants via the Voigt-Reuss-Hill approach [41,42]. For comparison, the experimental values of austenitic and ferritic steels are also listed in Table I [39,40]. For martensitic steels, experimental studies show that those share similar properties as ferritic steels with only 4% difference in the lattice constant and elastic moduli [40]. The values in Table I suggest that  $\alpha$ -Fe and ferritic steels share the similar lattice parameter and elastic constants. For austenitic steels, although they have the similar lattice parameter as  $\gamma$ -Fe, the elastic moduli of austenitic steels are twice as large as  $\gamma$ -Fe due to the large composition differences in austenitic steels compared to pure austenite.

The inclusion materials in this model are the group IVB (Ti, Zr, Hf), VB (V, Nb, Ta), and VIB (Mo, W) transition-metal carbides (TMCs). Most of these TMCs (excepting MoC and WC) are also known as interstitial compounds where the metal atoms form a close-packed metal sublattice and carbon atoms fill the interstices. Due to the order-disorder transition of carbon vacancies [43], the TMCs often exhibit a range of stoichiometries with  $0.5 \leq x \leq 1$  in  $\text{MC}_x$ . At 1:1 stoichiometry, the group IVB and VB TMCs have the rocksalt (B1) structure with a face-centered cubic (FCC) metal sublattice, while the group VIB TMCs have the Bh structure with a

TABLE I. The lattice constants and elastic constants of iron and steels, which were determined in experimental studies.

	Lattice parameter $a$ (Å)	Anisotropic elasticity $C_{ijkl}^M$ (GPa)			Isotropic elasticity	
		$C_{11}$	$C_{12}$	$C_{44}$	Young's modulus (GPa)	Poisson ratio $\nu$
$\gamma$ -Fe <sup>a</sup>	3.613	154 ± 14	122 ± 13	77 ± 8	112 ± 11	0.360 ± 0.036
$\alpha$ -Fe <sup>b</sup>	2.862	228 ± 2	132 ± 2	116	210 ± 2	0.287 ± 0.003
Austenitic steel <sup>c</sup>	3.530	209 ± 2	136 ± 1	130	266 ± 1	0.293 ± 0.013
Ferritic steel <sup>d</sup>	2.862	273.6 ± 0.3	82.10 ± 0.02	110.8 ± 0.3	210.3 ± 0.2	0.2877 ± 0.0003

<sup>a</sup>The lattice constants and anisotropic elastic constants were obtained from experimental studies in Ref. [34,36]. The Young's modulus and Poisson ratio were computed from  $C_{ijkl}^M$  using the Voigt-Reuss-Hill approach.

<sup>b</sup>The lattice constants and anisotropic elastic constants were obtained from experimental studies in Ref. [35,37,38]. The Young's modulus and Poisson ratio were computed from  $C_{ijkl}^M$  using the Voigt-Reuss-Hill approach.

<sup>c</sup>Single-crystal 70Fe-15Ni-15Cr in Ref. [39].

<sup>d</sup>Plain carbon steel, SAE 1050 with carbon composition of 0.5 wt% in Ref. [40].

simple hexagonal metal sublattice. Since the substoichiometric TMCs are carbon-vacancy-ordered structures, we categorize the carbides based on their metal-sublattice structures:  $MC_x$  with a FCC metal sublattice and  $MC_x$  with a hexagonal metal sublattice. In the following sections, results are shown and discussed corresponding to those two categories. In the group VIB and VB carbides, the B1 structure dominates for wide stoichiometries from MC to  $M_2C$  [43]. Between hemicarbides and monocarbides, two vacancy-ordered structures are included in this model,  $M_4C_3$  (space group C2c) [44,45] and  $M_3C_2$  (space group C2m), which are related to the B1 structure with a FCC metal sublattice. We are aware of other proposed structures of  $M_4C_3$  and  $M_3C_2$  [46,47] with a mixing FCC/HCP metal sublattice, such as the  $\zeta$  phase and  $\eta$  phase [48–51]. However, those structures are not investigated in this study since the  $\zeta$  phase and  $\eta$  phase are difficult to form and are not, to the authors knowledge, precipitates in steels. At 2:1 stoichiometry, the group IVB hemicarbides form the vacancy-ordered B1 structure (space group  $Fd\bar{3}m$  [43]) while the group VB and VIB hemicarbides form a hexagonal close packed (HCP) metal sublattice with carbon atoms filling the octahedral interstices with various configurations. In other words, the stacking sequence of the group VB and VIB hemicarbides is  $A\gamma_1B\gamma_2A \dots$ , where the different configurations in  $\gamma_1$  and  $\gamma_2$  planes [52] lead to different structures of those hemicarbides. Since most of the aforementioned stoichiometries of carbides  $MC_x$  have only been thoroughly investigated by *ab initio* calculations [52–54] while only a few verified in experiments [55–60], we use DFT calculations to obtain the consistent data for the lattice and elastic constants of the carbides.

For each carbide, DFT calculations were carried out in two steps using Vienna *ab initio* simulation package (VASP). At first, the conventional unit cell of the carbide was fully relaxed during the energy minimization process to determine the optimized structure associated with the minimum ground-state energy. Then, based on the optimized structure, the elastic constants were computed in VASP by applying the infinitesimal deformation on the relaxed lattice vectors. In our DFT calculations, we used the projector-augmented-wave (PAW) pseudopotentials [61,62] and the plane-wave basis with the energy cutoff 600 eV. The Perdew-Burke-Ernzerhof (PBE) formulation [63] and the generalized gradient approximation (GGA) method [64] were used to evaluate the electron

exchange correlation energy. To sample the Brillouin zone, the  $k$ -points density was set to be 55, which was equivalent to a  $12 \times 12 \times 12$   $k$ -point mesh for the conventional unit cell of carbides in the B1 structure. The first-order Methfessel-Paxton method was used for the Fermi-surface smearing with the smearing width 0.2 eV. The iteration criteria was set with the energy change of  $10^{-8}$  eV. It is worth noting that the structure and elasticity for each carbide from DFT calculations are based on the local coordinates defined in its conventional unit cell. Therefore, we provide the relaxed lattice vectors and the associated stiffness tensor in Table S1 within the Supplemental Material [32] for all carbides investigated. In addition, we compared our data with other published data for carbides [53], which were also obtained by DFT calculations using the PBE-GGA method. It is found that our data are consistent with the published data with only 5% difference.

### C. The elastic dipole of a H atom

The H atom also creates stress and strain fields inside the matrix which can be modeled using an elastic dipole tensor [29]. There are three methods that have been introduced to extract the elastic dipole from atomic-level simulations: the displacement fitting method [65], the homogeneous stress-strain method [66,67], and the Kanzaki force method [68]. Varvenne *et al.* implemented the aforementioned methods into the classical force-field atomic simulations and found that the elastic dipole obtained from three approaches converged to the same value when the simulation system was sufficiently large ( $> 10^4$  atoms) [69]. Nazarov *et al.* applied all three approaches to the *ab initio* calculations for a H atom in  $\alpha$ -Zr, where the simulation system was relatively small ( $\sim 10^2$  atoms) [70]. These authors compared the elastic dipole tensor extracted from DFT calculations with that determined in experiments [71] where upon they suggested that the homogeneous stress-strain method was optimal for small simulation systems in *ab initio* calculations. Therefore, the homogeneous stress-strain method is utilized in this study to compute the elastic dipole tensor of a H atom inside  $\alpha$ -Fe and  $\gamma$ -Fe. In this method, a homogenous strain field is applied to a region (simulation box) with a single point defect and the the elastic dipole tensor can be computed from the residual stress on the simulation box. When the residual stress tensor is allowed to relax to zero, the



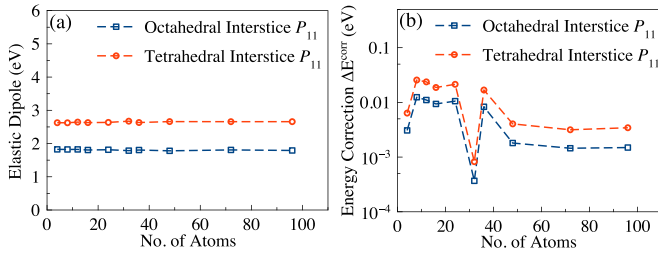


FIG. 2. (a) The components of the computed elastic dipole tensor for a H atom in  $\gamma$ -Fe as a function of the supercell size. The blue squares denote  $P_{11}$  for H at the octahedral interstices, and red circles denote  $P_{11}$  for H at the tetrahedral interstices. Due to the symmetry of  $\gamma$ -Fe, the elastic dipole tensor is isotropic  $P_{11} = P_{22} = P_{33}$ . (b) The energy correction term  $\Delta E^{\text{corr}}$  versus the supercell size.  $\Delta E^{\text{corr}}$  represents the energy correction to DFT calculations for the periodic images of the point defect. The blue squares represent  $\Delta E^{\text{corr}}$  for H at the octahedral interstices and red circles represent  $\Delta E^{\text{corr}}$  for H at the tetrahedral interstices.

elastic dipole components are computed as

$$P_{ij} = VC_{ijkl}^M \varepsilon_{kl}^h, \quad (8)$$

where  $V$  stands for the volume of the undistorted matrix,  $C_{ijkl}^M$  is the anisotropic stiffness tensor of the matrix, and  $\varepsilon_{kl}^h$  stands for the homogenous strain of the distorted matrix caused by the point defect. In this paper, we chose the experimental values of  $C_{ijkl}^M$  for  $\alpha$ -Fe and  $\gamma$ -Fe as listed in Table I. The volume  $V$  of the defect-free matrix and the homogeneous strain  $\varepsilon_{ij}^h$  of the distorted matrix were determined from DFT calculations. Using the same parameters in Sec. II B, the DFT calculations were carried out, for both  $\alpha$ -Fe and  $\gamma$ -Fe, to compute the ground-state energy of two structures: the iron matrix with and without an interstitial H atom. Based on the relaxed structure of the undistorted and distorted matrix, the homogeneous strain,  $\varepsilon_{kl}^h$  in Eq. (8), was computed from the deformation gradient  $\mathbf{F}$  using the Green-Lagrange strain definition:  $\mathbf{E}^{GL} = 1/2(\mathbf{F}^T \mathbf{F} - \mathbf{I})$ . Since the computed elastic dipole may depend on the size of the simulation cell, we examined the computed dipole as a function of the number of atoms in the simulation cell to establish the value of an isolated H atom. These supercells had 4, 8, 12, 16, 24, 32, 36, 48, 72, 96, 108 Fe atoms for  $\gamma$ -Fe while the supercells in  $\alpha$ -Fe had 2, 4, 6, 8, 12, 16, 18, 24, 36, 48, 54, 72, 96, 128, 160, 200, 250 Fe atoms.

The results of the computed elastic dipole tensor for a H atom inside  $\gamma$ -Fe as a function of the number of atoms are shown in Fig. 2(a). For H in both the octahedral and tetrahedral interstices, the values of  $P_{ij}$  converge within a variation of 0.05 eV for supercells with 96 atoms or more. These results also suggest that the elastic dipole tensor is isotropic  $P_{11} = P_{22} = P_{33}$ , as expected, which is due to the symmetry of the interstitial sites of the FCC structure. To make sure that the obtained  $P_{ij}$  is associated with an isolated (single) H atom, we used the anisotropic elasticity toolkit (ANETO) [72] to evaluate the interactions between the image point defects because of the periodic boundary condition in DFT calculations. This correction to the simulated formation energy, i.e.,  $\Delta E^{\text{corr}}$ , for H in  $\gamma$ -Fe is plotted in Fig. 2(b). The energy correction for the

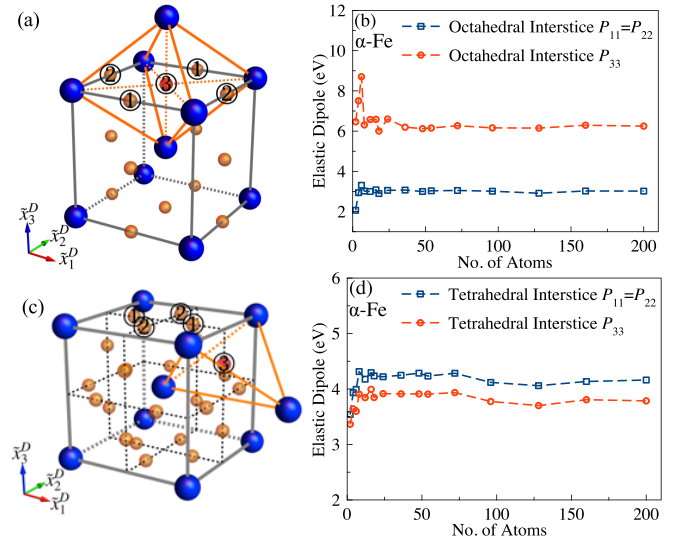


FIG. 3. (a) The octahedral interstices (orange spheres) in a conventional unit cell of  $\alpha$ -Fe with the defined local coordinates  $\tilde{x}_i^D$ . The three different interstitial positions are labeled as 1, 2, and 3, respectively. (b) The elastic dipole components of H at the octahedral P3 position, marked by the red sphere in (a), where  $P_{33} > P_{11} = P_{22}$ . (c) The tetrahedral interstices (orange spheres) in a conventional unit cell of  $\alpha$ -Fe with the defined local coordinates  $\tilde{x}_i^D$ . The three different interstitial positions are labeled as 1, 2, and 3, respectively. (d) The elastic dipole components of H at the tetrahedral P3 position, marked by the red spheres in (c), where  $P_{33} < P_{11} = P_{22}$ .

supercell with 96 atoms is below 5 meV, which is close to the precision expected for DFT simulations and thus the supercell with 96 atomic sites for  $\gamma$ -Fe with a H atom is sufficiently large. Therefore, the elastic dipole is  $P_{ij} = 1.79\delta_{ij}$  eV for a single H atom at an octahedral interstice and  $P_{ij} = 2.66\delta_{ij}$  eV for a tetrahedral-interstice H atom in  $\gamma$ -Fe.

For a H atom in  $\alpha$ -Fe, the elastic dipole tensor is anisotropic and depends on the interstitial position. For the atomic configuration shown in Fig. 3(a), the H atom at the octahedral position 3 has an elastic dipole tensor with nonzero diagonal components  $P_{33} > P_{11} = P_{22}$ , which converge within  $\pm 0.02$  eV for a supercell with 200 atoms. The larger magnitude component ( $P_{33}$ ) is due to the shorter distance to the octahedral vertices along the  $\tilde{x}_3^D$  direction. Similarly, the H atom at the tetrahedral position 3 in Fig. 3(c) has an elastic dipole tensor with nonzero diagonal components  $P_{33} < P_{11} = P_{22}$ , which converges within  $\pm 0.04$  eV for the supercell with 200 atoms. To ensure that the obtained elastic dipoles are for an isolated H atom, we computed the energy correction  $\Delta E^{\text{corr}}$ , which is less than 2 meV for the supercell with 200 atoms. For clarity, we label the three unique interstitial positions  $P_i$  (i.e., P1, P2, and P3) such that the elastic dipole components obey  $P_{ii} \neq P_{jj} = P_{kk}$ . For example, the elastic dipole components for H at the octahedral P3 position, which is (1/2, 1/2, 1) in the conventional  $\alpha$ -Fe unit cell, are  $P_{11} = P_{22} = 3.02$  eV,  $P_{33} = 6.25$  eV. The elastic dipole components for H at the tetrahedral P3, which is (1, 1/2, 3/4) in the conventional  $\alpha$ -Fe unit cell, are  $P_{11} = P_{22} = 4.16$  eV,  $P_{33} = 3.79$  eV. Finally, we note that the computed elastic dipole tensor is defined in the local coordinates of the  $\gamma$ -Fe

TABLE II. The orientation relationships between the carbide precipitates and the Fe matrix. In this paper, the normal vector of the coherent plane is parallel to  $\hat{x}_3$  in the global coordinate system.

Carbide metal sublattice	Matrix	Coherent Plane	Lattice-mismatch directions	
FCC	$\alpha$ -Fe	$(100)_{MC_x} \parallel (100)_\alpha$	$[011]_{MC_x} \parallel [010]_\alpha$	$[0\bar{1}1]_{MC_x} \parallel [001]_\alpha$
FCC	$\gamma$ -Fe	$(100)_{MC_x} \parallel (100)_\gamma$	$[010]_{MC_x} \parallel [010]_\gamma$	$[001]_{MC_x} \parallel [001]_\gamma$
Hexagonal	$\alpha$ -Fe	$(0001)_{MC_x} \parallel (011)_\alpha$	$[1\bar{1}00]_{MC_x} \parallel [0\bar{1}1]_\alpha$	$[11\bar{2}0]_{MC_x} \parallel [100]_\alpha$
Hexagonal	$\gamma$ -Fe	$(0001)_{MC_x} \parallel (111)_\gamma$	$[1\bar{1}00]_{MC_x} \parallel [112]_\gamma$	$[11\bar{2}0]_{MC_x} \parallel [110]_\gamma$

or  $\alpha$ -Fe structure. For H in  $\gamma$ -Fe, the elastic dipole tensor is isotropic, which is independent of the orientation of its local coordinates  $P_{ij} = \hat{P}_{ij}$ . For H in  $\alpha$ -Fe, the elastic dipole tensor  $\hat{P}_{ij}$  in the local coordinates  $\hat{x}_i^D$  has to be transformed into the quantity  $P_{ij}$  in the global coordinates  $\hat{x}_i$ .

At last, from these simulations, we can evaluate the energy differences (and hence favorability) of the types of interstices. The calculated ground-state energies of the Fe supercell with an interstitial H atom at the octahedral and tetrahedral interstices are denoted as  $E_o$  and  $E_t$ , respectively. The energy difference  $\Delta E_{ot} = E_o - E_t$  indicates the preference of the interstitial H and is useful in connecting the computed interaction energy to the binding energy (or trap energy) of H at the carbide interfaces. The results show that  $\Delta E_{ot} = -0.45$  eV in  $\gamma$ -Fe while  $\Delta E_{ot} = 0.13$  eV in  $\alpha$ -Fe, which means H atoms are more stable at the octahedral interstices in  $\gamma$ -Fe, but are more stable at the tetrahedral interstices in  $\alpha$ -Fe as expected [73]. (Please refer to the Supplemental Material [32] for the convergence study of  $\Delta E_{ot}$ ).

#### D. The eigenstrain of the carbide inclusion

The eigenstrains inside the carbide precipitates are not only a function of the lattice and elastic constants, but the orientation relationship (OR) that exists between the carbide and the matrix, and thus our model must also include information regarding these ORs. Carbide precipitates with an FCC metal sublattice in  $\gamma$ -Fe have the simple cube-on-cube OR  $\{100\}_{MC} \parallel \{100\}_\gamma$  [74] while the OR between these carbides and ferrite typically exhibit the Baker-Nutting OR [6], which we use in this study, with  $\{100\}_{MC} \parallel \{100\}_\alpha$ . The orientation relationship between the carbides with a hexagonal sublattice and ferritic steels ( $\alpha$ -Fe) was proposed by Pitsch *et al.* [75], known as the Pitsch-Schrader OR, where the slip plane in the matrix coincides with the close packed plane in the precipitate  $\{0001\}_{MC} \parallel \{011\}_\alpha$ . Although other orientation relationships between the HCP-structure precipitates and the BCC-structure matrix were observed by Jack, Burgers, and Potter [76,77], they all identified as having the same lattice-mismatch plane (coherent plane) as in the Pitsch-Schrader OR [78]. Thus, we chose the Pitsch-Schrader OR in this study for the coherent precipitates in  $\alpha$ -Fe and  $\gamma$ -Fe. Thus, the orientation relationships used in our model are listed in Table II and the eigenstrains of coherent carbide precipitates are computed accordingly.

As illustrated in Fig. 4(a), the coherent precipitate forms a small platelet, which can be viewed as an oblate spheroid with the semiaxes  $a_1 = a_2 > a_3$ . The interfaces of this oblate spheroidal precipitate (inclusion) are plotted schematically in Fig. 4(b) where the Baker-Nutting OR is adopted as an example. The broad surfaces of the inclusion form coherent

interfaces where a large eigenstrain is induced because of the lattice mismatch. On the surfaces near the edge of the oblate spheroid, the interface is incoherent where the lattice mismatch is negligible [79]. Therefore, according to the Baker-Nutting OR, the eigenstrain has nonzero components on the  $\hat{x}_1\hat{x}_2$  plane of the oblate spheroidal inclusion, which can be computed from the lattice mismatch along  $\langle 011 \rangle_{MC_x} \parallel \langle 010 \rangle_\alpha$  direction. In a similar way, the eigenstrains of all coherent carbide precipitates in  $\alpha$ -Fe and  $\gamma$ -Fe are computed based on ORs in Table II. We note that the obtained eigenstrains  $\tilde{\epsilon}_{ij}^{*}$  of the carbide particle is defined in the local coordinates of its conventional unit cell. Thus, we list the computed eigenstrains together with the associated lattice vectors within the Supplemental Material [32].

All the necessary physical quantities in this continuum model are determined via the methods discussed above. Using Eqs. (2)–(7), the elastic interaction energy  $E_{int}$  can be evaluated between a carbide particle and a H atom. To compute the interaction energies, these equations were implemented and evaluated in a computer program written in FORTRAN 90. Some approximations and simplifications of this continuum model are quantitatively investigated and elaborated upon in Appendix B.

### III. RESULTS AND DISCUSSION

#### A. The long-range hydrogen-binding capability of TiC

As stated previously, many experimental studies have found that disk-like coherent TiC precipitates have the potential to trap hydrogen and thus improve hydrogen tolerance

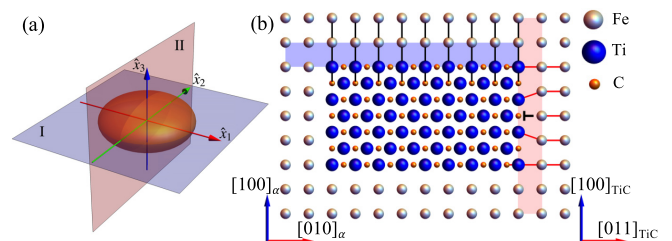


FIG. 4. A schematic of a coherent TiC precipitate in  $\alpha$ -Fe adopting the Baker-Nutting OR [7,16]. (a) A TiC platelet is modeled as an oblate spheroidal inclusion with the semiaxes  $a_1 = a_2 > a_3$  where the global coordinates  $\hat{x}_i$  are set along the semiaxes. (b) A schematic of the atomic configuration on the plane II in the subplot (a). Coherent interfaces (light-blue region) form on the broad surfaces of the oblate spheroid, which lead to the induced strain from the lattice mismatch. Near the edge of the oblate spheroid, incoherent interfaces (light-pink region) form and no significant strain is induced along the direction  $\hat{x}_3 \parallel [100]_\alpha \parallel [100]_{TiC}$ .

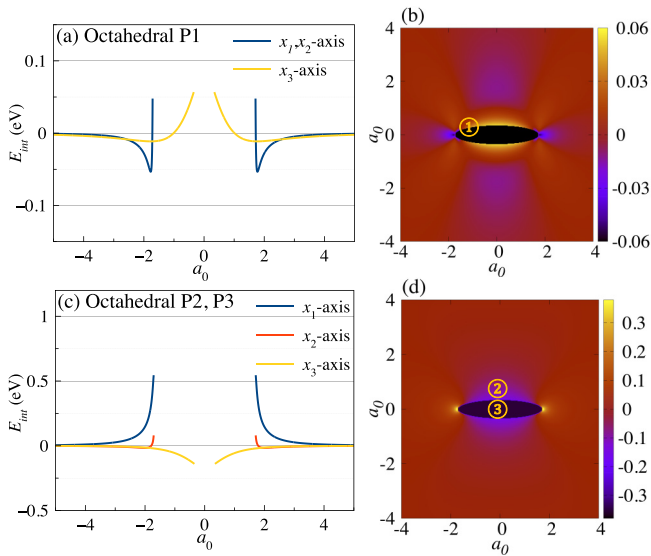


FIG. 5. The elastic interaction energy ( $E_{\text{int}}$ ) between the TiC oblate spheroidal inclusion ( $a_1 : a_3 = 5$ ) and a H atom in the octahedral interstice of  $\alpha$ -Fe. The Baker-Nutting OR is chosen where the plane normal of the coherent interface is  $\hat{x}_3 \parallel [100]_{\alpha} \parallel [100]_{\text{TiC}}$ . (a)  $E_{\text{int}}$  plotted along the semiaxes of the oblate spheroidal inclusion  $\hat{x}_i$  and (b)  $E_{\text{int}}$  plotted on the  $\hat{x}_1\hat{x}_3$  plane for H at the octahedral P1 position. (c)  $E_{\text{int}}$  plotted along the semiaxes of the oblate spheroidal inclusion  $\hat{x}_i$  and (d)  $E_{\text{int}}$  plotted on the  $\hat{x}_1\hat{x}_3$  plane for H at the octahedral P2 and P3 positions. In the subplots (b) and (d), the circled numbers show the site at the inclusion interface associated with the largest hydrogen-binding energy.

of steels [5,7,16]. Thus, we choose to use the results for the  $E_{\text{int}}$  between TiC particles and H as an illustrative example of the interaction between the FCC structured carbides and H atoms. The small platelet of the coherent TiC precipitate is modeled as an oblate spheroidal inclusion with the semi-axes  $a_1 : a_3 = 5$ , which is in agreement with the aspect ratios reported experimentally [7]. The elastic interaction energy between the TiC inclusion and hydrogen  $E_{\text{int}}$  was computed as a function of position in the region  $-5a_0 \leq x, y, z \leq 5a_0$ , where  $a_0 = (a_1 a_2 a_3)^{1/3}$  is the characteristic length of the inclusion. This was done in both  $\gamma$ -Fe and  $\alpha$ -Fe.

The interaction energies for  $\alpha$ -Fe are plotted in Fig. 5 and Fig. 6 for H at the octahedral and tetrahedral interstices, respectively. The first observation one can make from the plots is that  $E_{\text{int}}$  decays as  $1/r^3$  where  $r$  is the distance between hydrogen and the carbide inclusion, which means the hydrogen-binding capability is only significant near the carbide interfaces. This is expected and is a direct result of the nature of the elastic interactions between two sources of strain, but ensures all the other major conclusions of this paper can be obtained by only examining  $E_{\text{int}}$  at the surface. For a given ellipsoidal inclusion, the interaction energy  $E_{\text{int}}$  for hydrogen is negligible when it is about  $5a_0$  away from the inclusion, where  $a_0 = (a_1 a_2 a_3)^{1/3}$  is the characteristic length of the inclusion. The second point worth noting is that due to the Baker-Nutting OR in ferrite and the cube-on-cube in austenite, the eigenstrain in the coherent plane is isotropic ( $\tilde{\epsilon}_{11}^* = \tilde{\epsilon}_{22}^*$ ), which results in the P2 and P3 being equivalent

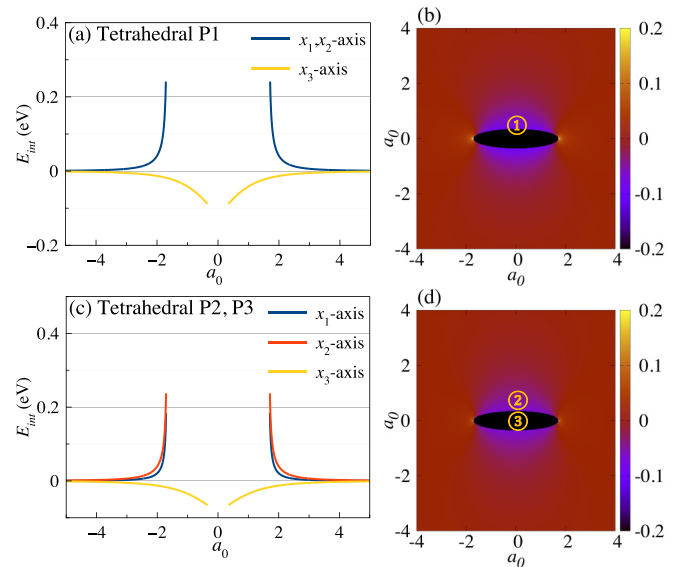


FIG. 6. The elastic interaction energy  $E_{\text{int}}$  between the TiC oblate spheroidal inclusion ( $a_1 : a_3 = 5$ ) and a H atom in the tetrahedral interstice of  $\alpha$ -Fe. The Baker-Nutting OR is chosen where the plane normal of the coherent interface is  $\hat{x}_3 \parallel [100]_{\alpha} \parallel [100]_{\text{TiC}}$ . (a)  $E_{\text{int}}$  plotted along the semiaxes of the oblate spheroidal inclusion  $\hat{x}_i$  and (b)  $E_{\text{int}}$  plotted on the  $\hat{x}_1\hat{x}_3$  plane for H at the tetrahedral P1 position. (c)  $E_{\text{int}}$  plotted along the semiaxes of the oblate spheroidal inclusion  $\hat{x}_i$  and (d)  $E_{\text{int}}$  on the  $\hat{x}_1\hat{x}_3$  plane for H at the tetrahedral P2 and P3 positions. In the subplots (b) and (d), the circled numbers represent the point at the inclusion interface associated with the largest hydrogen-binding energy.

and thus we only have to analyze two different orientations for each interstice. It is worth noting that  $E_{\text{int}}$  for the octahedral P2 is much larger than that for the octahedral P1 at the vertices  $(\pm a_1, 0, 0)$  as shown in Figs. 5(a) and 5(c), which is attributed to the coupling between the anisotropic elastic dipole and the large contractive strain near the edge of the inclusion platelet.

Figures 5(b) and 5(d) demonstrate that H is subjected to a repulsive force ( $E_{\text{int}} > 0$ ) near the broad interface of the TiC platelet when H is at the octahedral P1 but an attractive force ( $E_{\text{int}} < 0$ ) when H is at the octahedral P2 and P3 (the numbering scheme is denoted in Fig. 3). For H at the tetrahedral interstices, Figures 6(b) and 6(d), the H atoms are attracted to the broad interface of the TiC platelet for all three unique tetrahedral positions. Noting that the magnitude of  $E_{\text{int}}$  is much larger for the octahedral P2 and P3 positions than the P1 position, our results suggest that hydrogen is attracted to the broad surface of the TiC platelet, which is consistent with the experimental observations by Takahashi *et al.* [16]. However, Takahashi *et al.* concluded that the hydrogen-binding effect was not related to the strain field since the hydrogen-binding sites were away from the edge of the TiC platelet where the strains are the largest. The authors correctly noted the strains would be the largest at the edges of the platelets, at the vertices  $(\pm a_1, 0, 0)$  and  $(0, \pm a_2, 0)$  in Figs. 6(a) and 6(c), and thus would result in the largest interaction. However Takahashi *et al.* neglected the sign whereas our results clearly demonstrate that hydrogen interstitials are repelled from the

edge of the disk and thus should not bind to this area. The presence of a H atom generally creates a positive dilatational strain field in the matrix and the large positive strains inside the inclusion cause the contraction in the nearby matrix at the edge of the oblate spheroidal inclusion,  $(\pm a_1, 0, 0)$ , which leads to a repulsive force on H atoms in this region. Finally, we note the magnitude of  $E_{\text{int}}$  at the co-vertices of the broad face, i.e.,  $(0, 0, \pm a_3)$ , is about 0.1 eV, which suggests a weak hydrogen-binding capability. However, the difference in  $E_{\text{int}}$  between the vertices and covertices is about 0.4 eV, which ensures the broad surfaces of the TiC platelet are preferred hydrogen-binding sites.

To quantitatively evaluate the hydrogen-binding capability, we investigated the position and value of the minimum elastic-strain interaction energy  $E_{\text{int}}(\text{min})$  at the interfaces of the TiC platelet. To do so, we computed  $E_{\text{min}}$  at points  $(x_1, x_2, x_3)$  on the inclusion surface by changing the parameters  $(u, v)$  every  $2^\circ$  where

$$x_1 = a_1 \cos u \sin v, \quad x_2 = a_2 \sin u \sin v, \quad x_3 = a_3 \cos v, \quad (9)$$

with  $u \in [0, 2\pi)$  and  $v \in [0, \pi)$ . The site associated with  $E_{\text{int}}(\text{min})$ , or the strongest hydrogen-binding capability, at the inclusion interface is labeled in Fig. 5 and Fig. 6 for all configurations of an interstitial H atom. When H is at the octahedral P1, the strongest hydrogen-binding sites are near the edge of the oblate spheroidal inclusion where  $v = 78^\circ$  and  $E_{\text{int}}(\text{min}) = -0.085$  eV. When H is at the octahedral P2/P3, the strongest hydrogen-binding point is at the covertices  $(0, 0, \pm a_3)$  where  $v = 0^\circ$  and  $E_{\text{int}}(\text{min}) = -0.140$  eV. For H at the tetrahedral interstices, the covertices,  $(0, 0, \pm a_3)$ , are always the strongest hydrogen-binding sites where  $E_{\text{int}}(\text{min}) = -0.089$  eV and  $E_{\text{int}}(\text{min}) = -0.066$  eV for H at the tetrahedral P1 and tetrahedral P2/P3, respectively. In this study, among all unique interstitial positions, the lowest value in  $E_{\text{int}}(\text{min})$  is chosen to represent the hydrogen-binding capability. Therefore, for the oblate spheroidal TiC precipitate with  $a_1 : a_3 = 5$ , we report  $E_{\text{int}}(\text{min}) = -0.140$  eV for H at the octahedral interstices and  $E_{\text{int}}(\text{min}) = -0.089$  eV for H at the tetrahedral interstices. In Ref. [80], Di Stefano *et al.* studied the interactions between H and TiC inside  $\alpha$ -Fe by performing DFT simulations. The study suggested that both the elastic-strain energy and the local atomic configuration play important roles in H binding capability. By removing chemical effects, the elastic-strain energy for the tetrahedral-interstitial H atom was evaluated to be  $-0.18$  eV on an infinite-plane interface with the plane normal  $[001]_\alpha \parallel [001]_{\text{TiC}}$ . To compare with the reported data [80], we evaluated the long-range elastic interaction for a spherical inclusion since an infinite plane is equivalent to a sphere with an infinite radius. The values of  $E_{\text{int}}(\text{min})$  between a tetrahedral-interstitial H atom and a spherical TiC inclusion are  $-0.192$  eV for position P1 and  $-0.153$  eV for position P2/P3, which are close to their reported data indicating our continuum model can accurately model the elastic interactions of hydrogen and carbide precipitates.

For H at the octahedral or tetrahedral interstices in  $\gamma$ -Fe,  $E_{\text{int}}$  is independent of the H atom position since the elastic dipole tensor is isotropic. As shown in Fig. 7, the broad surfaces of the TiC platelet are energetically favorable for H atoms and the covertices  $(0, 0, \pm a_3)$  are the interfacial sites

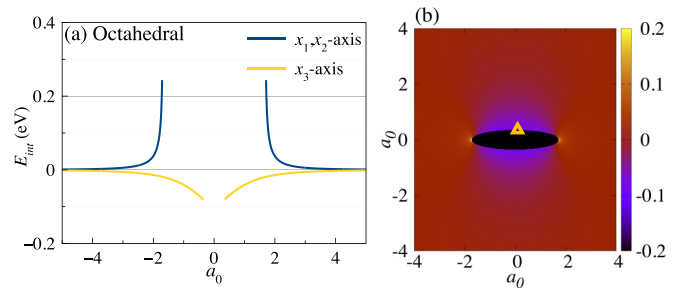


FIG. 7. The elastic interaction energy  $E_{\text{int}}$  between the TiC oblate spheroidal inclusion ( $a_1 : a_3 = 5$ ) and a H atom in the octahedral interstice of  $\gamma$ -Fe. (a)  $E_{\text{int}}$  plotted along the semiaxes of the oblate spheroidal inclusion  $\hat{x}_i$  and (b)  $E_{\text{int}}$  plotted on the  $\hat{x}_1\hat{x}_3$  plane. The orange-triangle marks the site at the inclusion interface associated with the largest hydrogen-binding energy.

associated to the strongest hydrogen-binding capability, which is  $E_{\text{int}}(\text{min}) = -0.0810$  eV for an octahedral-interstice H. For tetrahedral-interstice H atoms, the result only differs from that for an octahedral interstices by a scale factor, which results in  $E_{\text{int}}(\text{min}) = -0.120$  eV at  $(0, 0, \pm a_3)$ .

## B. The carbides with a FCC metal sublattice in Fe

Using the same procedures outlined in Sec. III A, the minimum interaction energy  $E_{\text{int}}(\text{min})$  was computed for all B1-based carbides when the shape of the coherent precipitate is an oblate spheroid with  $a_1 : a_3 = 5$ . The elastic interaction energy  $E_{\text{int}}$  for all the B1-based carbides exhibits similar patterns to that of TiC, which are illustrated in Figs. 5–7 and thus we do not present these individual spacial results for each element. To facilitate comparisons of the hydrogen binding (or trapping) capability among the different carbides, the lowest value of  $E_{\text{int}}(\text{min})$  in each carbide is plotted in Fig. 8 for the two types of interstices (octahedral and tetrahedral) inside the two matrix materials ( $\alpha$ -Fe and  $\gamma$ -Fe). These results include the variation of carbon concentration, which was evaluated using the elastic constants and lattice constants of the carbide structures discussed in Sec. II B.

The examination of Fig. 8 reveals several general trends regarding the binding of H to carbide precipitates in the cubic carbides that are worth noting. First, the interaction energy of octahedral interstices is stronger than tetrahedral interstices in  $\alpha$ -Fe. Similarly, we can see that the tetrahedral interstices have a stronger interaction energy with the carbides in  $\gamma$ -Fe. In each of these cases, the stronger interaction energy (larger in magnitude) is associated with the less stable interstice, which generally has a larger elastic dipole, creating a larger magnitude elastic interaction. This would appear to imply that there is a stronger hydrogen binding energy for the octahedral interstices in  $\alpha$ -Fe. However, this is not true since the elastic interaction energies for the two interstices have different references, which must be corrected to identify the binding energy of a H atom to the carbide interface. Since the tetrahedral interstices are the more favorable bulk interstitial site in  $\alpha$ -Fe and the octahedral interstices are more favorable in  $\gamma$ -Fe, these are the correct reference to compute the binding energies. Thus, the hydrogen binding energies to



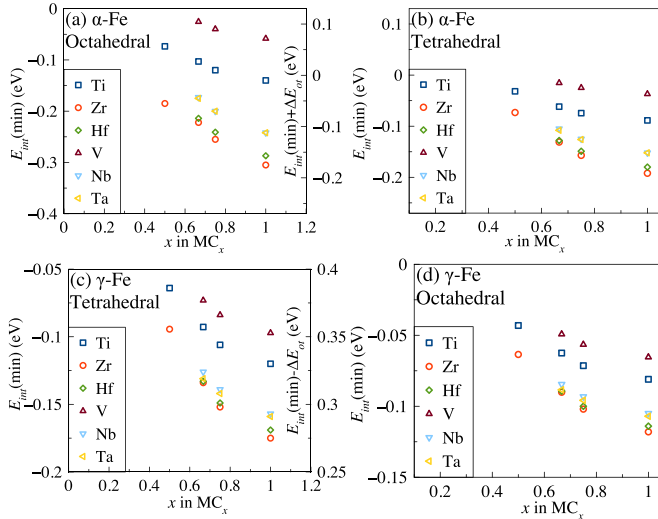


FIG. 8. The minimum elastic interaction energy  $E_{\text{int}}$  on the surface of an oblate spheroidal inclusion ( $a_1 : a_3 = 5$ ) for the carbides with a FCC metal sublattice plotted as a function of the carbon concentration. (a) H at the octahedral interstices inside  $\alpha$ -Fe; (b) H at the tetrahedral interstices inside  $\alpha$ -Fe; (c) H at the tetrahedral interstices inside  $\gamma$ -Fe; (d) H at the octahedral interstices inside  $\gamma$ -Fe. In the subplot (a), the right-vertical axis represents the elastic-strain interaction energy referenced to the ground-state energy of the tetrahedral-interstice H atom,  $E_{\text{int}}(\text{min}) + \Delta E_{\text{or}}$ . In the subplot (c), the right-vertical axis represents the elastic-strain interaction energy referenced to the ground-state energy of the octahedral-interstice H atom,  $E_{\text{int}}(\text{min}) - \Delta E_{\text{or}}$ .

the interface for  $\alpha$  and  $\gamma$ -Fe are referenced to their respective favorable interstices. The binding energies for octahedral H interstitials in  $\alpha$ -Fe and tetrahedral H interstitials in  $\gamma$ -Fe should be referenced using the right vertical axis in Figs. 8(a) and 8(c), i.e.,  $E_{\text{int}}(\text{min}) \pm \Delta E_{\text{or}}$ , while the binding energies for tetrahedral H interstitials in  $\alpha$ -Fe and octahedral H interstitials in  $\gamma$ -Fe are equal to  $E_{\text{int}}$ , the left axis in Figs. 8(b) and 8(d). These results indicate that in  $\alpha$ -Fe, H atoms can be at either the octahedral or tetrahedral interstices near the covertices of the coherent carbide platelet since they have similar binding energies. In contrast, the octahedral interstice near the broad face of precipitates in  $\gamma$ -Fe are still more stable even though the attractive elastic interaction is larger for the tetrahedral-interstice H. Second, we note that there is a stronger interaction energy between H atoms and carbides in ferrite compared to that in austenite. This is a combination of the larger dipole moments of H atoms in  $\alpha$ -Fe and the larger elastic constants of  $\alpha$ -Fe.

As shown in Fig. 8, for stoichiometric carbides with the same metal element,  $|E_{\text{int}}(\text{min})|$  decreases gradually with respect to the decreasing carbon concentration ( $x$  in  $\text{MC}_x$ ). Such a trend is attributed primarily to the decrease in the elastic moduli of B1-structure based carbides caused by the increase in carbon vacancies. For carbides at the same carbon composition, the magnitude of the interaction energy, which characterizes its hydrogen trapping ability, follows  $\text{ZrC}_x > \text{HfC}_x > \text{TaC}_x \simeq \text{NbC}_x > \text{TiC}_x > \text{VC}_x$ , which is consistent with the experimental findings comparing TiC, NbC, and TaC [7]. This trend can primarily be explained, as noted in [7],

by the magnitude of the lattice mismatch between the matrix and the carbide particles. Thus, these results clearly show that stoichiometric carbides of zirconium and hafnium should be the most favorable in trapping hydrogen at their surface due to the elastic interactions.

### C. The carbides with a hexagonal metal sublattice in Fe

In this study, the carbides with a hexagonal metal sublattice include the group VIB MC (Bh structure, space group  $P\bar{6}m2$ ), the group VB and VIB  $\text{M}_2\text{C}$  (space groups  $P\bar{3}m1$ ,  $P\bar{3}1m$ ,  $Pbcn$ ,  $Pnma$ ,  $Pnmm$ ). Those carbides share similarities in many aspects, including the lattice, symmetry of elastic constants, and the orientation relationship with the matrix, which lead to the similar results of the elastic-strain interaction energy  $E_{\text{int}}$ . However, we do note that the metal atoms stacking differently based on chemistry. The group VIB MCs stack with a simple hexagonal repeat and thus are not close-packed, while the group VB and VIB  $\text{M}_2\text{C}$ s arrange in a HCP substructure and are, in fact, close-packed. Hereby, we illustrate and discuss the results of  $E_{\text{int}}$  between WC and H as an example. The coherent WC precipitate is modeled as the oblate spheroidal inclusion with the semiaxes  $a_1 : a_3 = 5$  where the Pitsch-Schrader OR is adopted:  $\hat{x}_3 \parallel [0001]_{\text{WC}} \parallel [011]_{\alpha}$  and  $\hat{x}_3 \parallel [0001]_{\text{WC}} \parallel [111]_{\gamma}$ .

For the WC precipitate in  $\alpha$ -Fe, the interaction energy  $E_{\text{int}}$  is computed at the points  $(x, y, z)$  in the region  $-5a_0 \leq x, y, z \leq 5a_0$  for the three unique interstitial positions of H. When H is at the interstitial positions P2 and P3, the values of  $E_{\text{int}}$  are the same along the semiaxes of the inclusion  $\hat{x}_i$ , but have slight differences at other positions, which is due to the anisotropic eigenstrains on the coherent plane ( $\bar{\epsilon}_{11}^I \neq \bar{\epsilon}_{22}^I$ ). Figure 9 shows that when H is at the octahedral P1 position, the magnitude of  $E_{\text{int}}$  is much larger than that when H is at the octahedral P2/P3 position. Thus, for H at the octahedral interstices inside  $\alpha$ -Fe, the broad surfaces of the WC platelet are the preferred hydrogen-binding sites. Similar to what was done in the cubic carbides, the interfacial sites associated with the largest long-range hydrogen-binding energy are determined by varying the parameters  $(u, v)$  in Eq. (9). The lowest value of  $E_{\text{int}} = -0.466$  eV is located at the interfacial sites  $(0, 0, \pm a_3)$  for H at the octahedral P1 position.

The interaction energy  $E_{\text{int}}$  between the WC precipitate and H at the tetrahedral interstices in  $\alpha$ -Fe is plotted in Fig. 10. Similar patterns of  $E_{\text{int}}$  are found for H at all three unique interstitial positions (P1, P2, and P3), where attractive interactions occur along the  $\hat{x}_1$  and  $\hat{x}_3$  directions while repulsive interactions occur along the  $\hat{x}_2$  direction. These results also indicate that the broad surfaces of the WC platelet are energetically favorable for H atoms at the tetrahedral interstices. When H is at the tetrahedral P1 and P2 positions, the interfacial sites for  $E_{\text{int}}(\text{min})$  are the covertices  $(0, 0, \pm a_3)$  with  $E_{\text{int}}(\text{min}) = -0.130$  eV and  $-0.182$  eV, respectively. When H is at the tetrahedral P3 position, the interfacial sites for  $E_{\text{int}}(\text{min})$  move to the points where  $v = 60^\circ$  and  $E_{\text{int}}(\text{min}) = -0.194$  eV, which is similar to the value for H at the tetrahedral P2 position. Therefore, the quantitative values for the hydrogen-binding capability of the coherent WC precipitate inside  $\alpha$ -Fe are  $E_{\text{int}}(\text{min}) = -0.466$  eV for

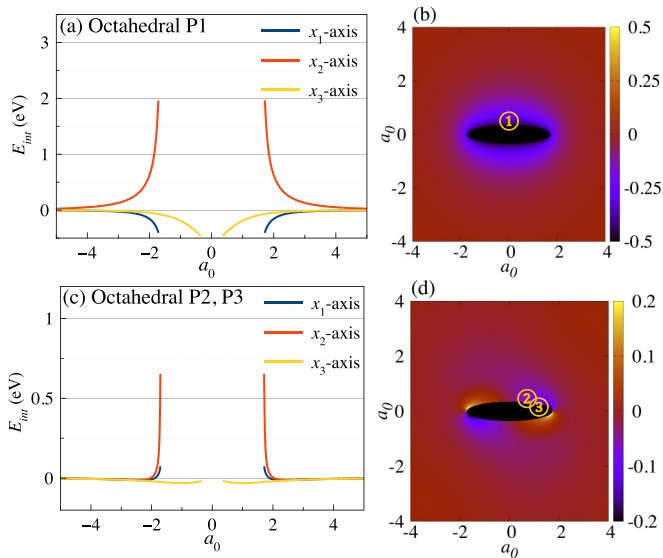


FIG. 9. The elastic interaction energy  $E_{\text{int}}$  between the WC oblate spheroidal inclusion ( $a_1 : a_3 = 5$ ) and a H atom in the octahedral interstice of  $\alpha$ -Fe. The Pitsch-Shrader OR is chosen where the plane normal of the coherent interface is  $\hat{x}_3 \parallel [001]_{\alpha} \parallel [0001]_{\text{WC}}$  (a)  $E_{\text{int}}$  plotted along the semiaxes of the oblate spheroidal inclusion  $\hat{x}_i$  and (b)  $E_{\text{int}}$  plotted on the  $\hat{x}_1\hat{x}_3$  plane for H at the octahedral P1 position. (c)  $E_{\text{int}}$  plotted along the semiaxes of the oblate spheroidal inclusion  $\hat{x}_i$  for H at the octahedral P2 and P3 positions; (d)  $E_{\text{int}}$  plotted on the  $\hat{x}_1\hat{x}_3$  plane for H at the octahedral P2 position. In the subplots (b) and (d), the circled numbers show the site at the inclusion interface associated with the largest hydrogen-binding energy.

the octahedral-interstice H and  $E_{\text{int}}(\text{min}) = -0.194$  eV for the tetrahedral-interstice H.

For the WC precipitate in  $\gamma$ -Fe, the values of  $E_{\text{int}}$  are plotted in Fig. 11 for H at the octahedral interstices noting that the results for  $E_{\text{int}}$  of the tetrahedral interstices are just scaled versions of these plots. Figure 11 shows that H atoms tend to be attracted near the broad surfaces of the WC platelet inside  $\gamma$ -Fe. At the covertips ( $0, 0, \pm a_3$ ), the long-range hydrogen-binding capability is the strongest where  $E_{\text{int}}(\text{min}) = -0.0626$  eV and  $-0.0931$  eV for the octahedral-interstice H and tetrahedral-interstice H, respectively.

Given the same inclusion shape ( $a_1 : a_2 : a_3 = 5 : 5 : 1$ ), the values of  $E_{\text{int}}(\text{min})$  were computed for all the carbides with a hexagonal metal sublattice. As noted previously, the group VB and VIB hemicarbides adopt different structures and have polymorphic phase transitions with temperature requiring examination of all the aforementioned structures for the hemicarbides. We note that the computed  $E_{\text{int}}$  of these different structures is actually quite similar for a given composition and thus we plot the average result in Fig. 12 to represent the hydrogen-binding capability for each hemicarbide. The right axes in Figs. 12(a) and 12(c) correct the interaction energy to represent a binding energy of the most favorable isolated interstitial in that iron structure so that it is equivalent to a hydrogen binding or trap energy. Several trends of the hydrogen-binding effectiveness are observed in Fig. 12. First, the magnitude of  $|E_{\text{int}}(\text{min})|$  in  $\alpha$ -Fe is larger than that in  $\gamma$ -Fe because of the larger elastic moduli of  $\alpha$ -Fe. Furthermore,

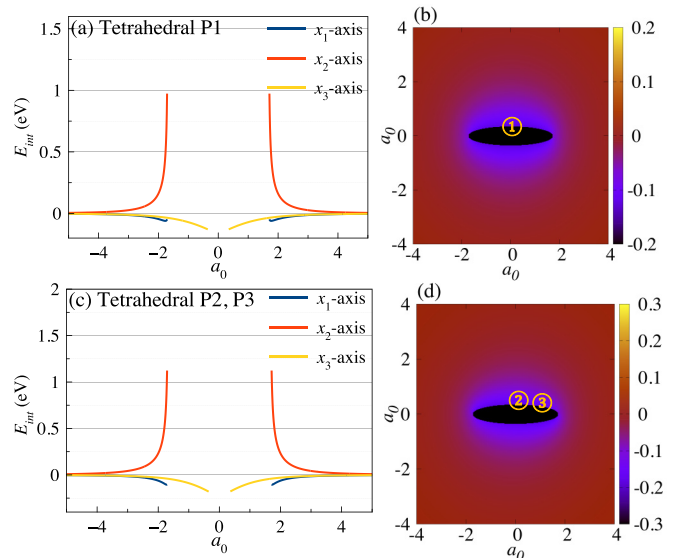


FIG. 10. The elastic interaction energy  $E_{\text{int}}$  between the WC oblate spheroidal inclusion ( $a_1 : a_3 = 5$ ) and a H atom in the tetrahedral interstice of  $\alpha$ -Fe. The Pitsch-Shrader OR is chosen where the plane normal of the coherent interface is  $\hat{x}_3 \parallel [001]_{\alpha} \parallel [0001]_{\text{WC}}$ . (a)  $E_{\text{int}}$  plotted along the semiaxes of the oblate spheroidal inclusion  $\hat{x}_i$  and (b)  $E_{\text{int}}$  plotted on the  $\hat{x}_1\hat{x}_3$  plane for H at the tetrahedral P1 position. (c)  $E_{\text{int}}$  plotted along the semiaxes of the oblate spheroidal inclusion  $\hat{x}_i$  for H at the tetrahedral P2 and P3 positions and (d)  $E_{\text{int}}$  plotted on the  $\hat{x}_1\hat{x}_3$  plane for H at the tetrahedral P2 position. In the subplots (b) and (d), the circled numbers represent the point at the inclusion interface associated with the largest hydrogen binding energy.

the group VIB hemicarbides ( $\text{Mo}_2\text{C}$  and  $\text{W}_2\text{C}$ ) have better hydrogen-binding capability than the monocarbides (MoC and WC), which is attributed to the larger eigenstrains of those hemicarbides. Moreover, the group VB and VIB hemicarbides are promising for the hydrogen trapping except for  $\text{V}_2\text{C}$ , which has the relatively low hydrogen-binding energy due to its small eigenstrains. If one references the binding energy, the H atoms will likely bind at the octahedral interstices that are near the covertips of the coherent carbide platelet because of the large magnitude of the elastic-strain interaction energy  $E_{\text{int}}$

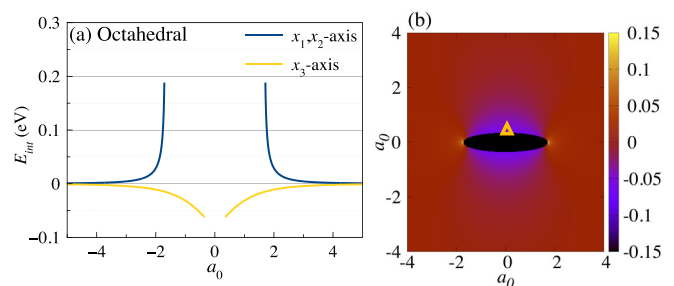


FIG. 11. The elastic interaction energy  $E_{\text{int}}$  between the WC oblate spheroidal inclusion ( $a_1 : a_3 = 5$ ) and a H atom in the octahedral interstice of  $\gamma$ -Fe. (a)  $E_{\text{int}}$  plotted along the semiaxes of the oblate spheroidal inclusion  $\hat{x}_i$  and (b)  $E_{\text{int}}$  plotted on the  $\hat{x}_1\hat{x}_3$  plane. The orange triangle marks the site at the inclusion interface associated with the largest long-range hydrogen binding energy.

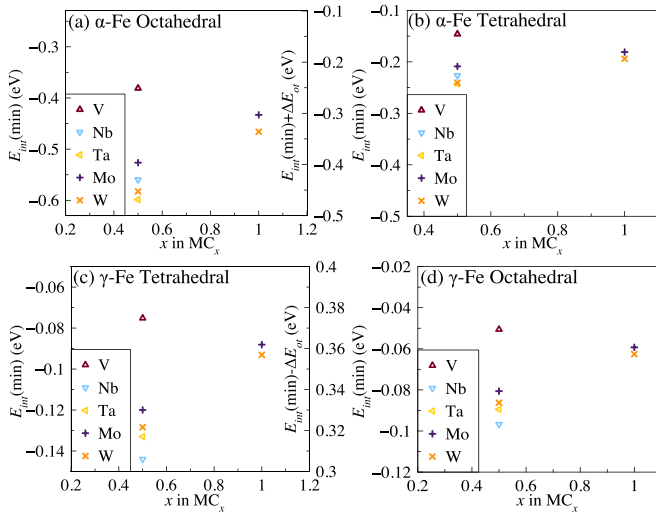


FIG. 12. The minimum elastic interaction energy  $E_{\text{int}}$  on the surface of an oblate spheroidal inclusion ( $a_1 : a_3 = 5$ ) for the carbides with a hexagonal metal sublattice plotted as a function of carbon concentration. (a) H at the octahedral interstices inside  $\alpha$ -Fe; (b) H at the tetrahedral interstices inside  $\alpha$ -Fe; (c) H at the tetrahedral interstices inside  $\gamma$ -Fe; and (d) H at the octahedral interstices inside  $\gamma$ -Fe. In the subplot (a), the right-vertical axis represents the elastic-strain interaction energy referenced to the ground-state energy of the tetrahedral-interstice H atom,  $E_{\text{int}}(\text{min}) + \Delta E_{\text{el}}$ . In the subplot (c), the right-vertical axis represents the elastic-strain interaction energy referenced to the ground-state energy of the octahedral-interstice H atom,  $E_{\text{int}}(\text{min}) - \Delta E_{\text{el}}$ .

in  $\alpha$ -Fe. Thus, for the hexagonal carbide precipitates in ferrite, the hydrogen interstitials prefer the tetrahedral interstices in the bulk but octahedral interstices at the ferrite-carbide interface. In  $\gamma$ -Fe, the octahedral interstices are still the preferable sites for H atoms near the broad surface of the coherent carbide platelet. All data shown in Fig. 8 and Fig. 11 are listed in Table S2 within the Supplemental Material [32].

#### D. Changes in $E_{\text{int}}$ due to morphologies and sizes

The results of  $E_{\text{int}}$  discussed previously are based on small platelet-shaped coherent precipitates. As the coherent precipitate grows, both the diameter and the thickness of the platelet increase and the platelet gradually becomes an ellipsoid with a reduced eccentricity [7]. A detailed discussion of the standard growth pattern for carbide precipitates is covered within the Supplemental Material [32]. To understand how changes in morphology would affect the computed interaction energies, we investigated the hydrogen-binding capability of the oblate spheroidal inclusions with the varying eccentricity,  $\sqrt{a_1^2 - a_3^2}/a_1$ , by changing the  $a_1/a_3$  ratio. As illustrative examples, the results of TiC and WC are shown in Fig. 13 for the carbides with the FCC and hexagonal metal sublattices, respectively.

For the same carbide, there are two trends of  $E_{\text{int}}(\text{min})$  shown in Fig. 13, which depend on the anisotropy in elastic dipole tensors. When the interfacial sites for  $E_{\text{int}}(\text{min})$  are on the broad surface of the oblate spheroidal inclusion, the curves of  $E_{\text{int}}(\text{min})$  are positively related to the ratio  $a_1/a_3$

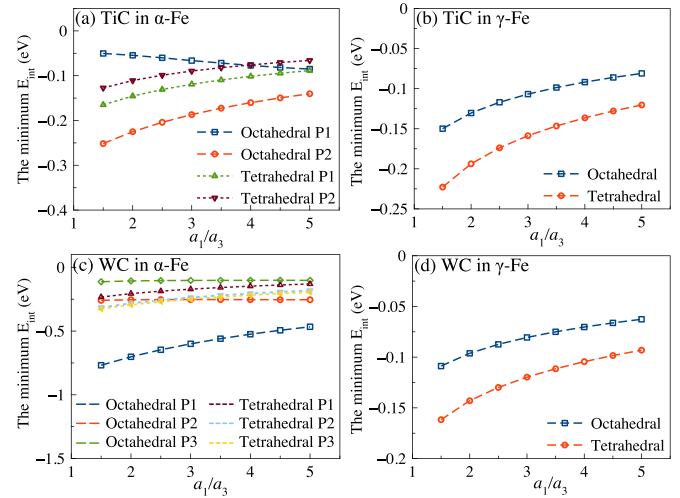


FIG. 13. The values of  $E_{\text{int}}(\text{min})$  for oblate spheroidal inclusions with  $a_1/a_3$  ranging from 1.5 to 5. (a) The TiC coherent precipitate in  $\alpha$ -Fe; (b) the TiC coherent precipitate in  $\gamma$ -Fe; (c) the WC coherent precipitate in  $\alpha$ -Fe; (d) the WC coherent precipitate in  $\gamma$ -Fe.

or the eccentricity. In contrast, when the interfacial sites for  $E_{\text{int}}(\text{min})$  are near the edge of the oblate spheroidal inclusion, the curves of  $E_{\text{int}}(\text{min})$  are negatively related to the  $a_1/a_3$  ratio. For example, as the TiC coherent precipitate grows in  $\alpha$ -Fe, this oblate spheroidal inclusion changes its shape by decreasing its eccentricity,  $\sqrt{a_1^2 - a_3^2}/a_1$ . When it occurs, the hydrogen-binding capability of TiC becomes weaker for H at the octahedral P1, but becomes stronger for H at the octahedral P2/P3. Noting that the magnitude of  $E_{\text{int}}(\text{min})$  is larger for H at the octahedral P2/P3, the hydrogen-binding capability of the coherent TiC precipitate increases with respect to the decreasing eccentricity of the precipitate. The same patterns are observed for WC where the curve associated with the strongest H binding capability (octahedral P1) indicates the negative correlation between  $|E_{\text{int}}(\text{min})|$  and the eccentricity. The slopes of the curves for the P1 in WC is different from that of TiC, because, due to the different ORs, P1 in WC binds to the broad face of the carbide platelet rather than P1 in TiC is located near the edge of the carbide platelet.

These results suggests that the growth of the coherent carbide precipitate will increase its hydrogen-binding effectiveness because of two reasons. First, since the broad surfaces are the energetically favorable sites for H atoms, larger precipitate have more interfacial area for the hydrogen to bind. Second, the eccentricity of the coherent precipitate decreases towards zero (sphere) as it grows, which results in the increasing negative value of  $E_{\text{int}}(\text{min})$ , which is equivalently the increasing hydrogen-binding capability of the precipitate. It is worth noting that our conclusion about the shape and size effects in the hydrogen-binding capability is consistent with the experimental observations [7,13]. However, we also note that these trends do not account for changes in the coherency of the interface that also changes as the precipitate grows. The growth of a precipitate typically reduces the magnitude of the coherency strains and eventually reduces the overall interaction to zero when the particle is incoherent, which is now discussed with associated details in the following section.



### E. Changes in $E_{\text{int}}$ due to interface characteristics

As noted above, when the growth of a coherent precipitate continues, an oblate spheroidal coherent precipitate gradually changes into an ellipsoidal semicoherent precipitate, which finally becomes a spherical incoherent precipitate [7]. For a semicoherent precipitate, on the semicoherent interface, the eigenstrain is associated with partial lattice mismatch, which is not usually known. Furthermore, as the precipitates become semicoherent, the precipitates do not strictly follow the Baker-Nutting OR. Thus, it can be difficult to fully evaluate the role of strain energy and its ability to interact with H atoms.

In this section, we choose to investigate the lower bound of  $E_{\text{int}}$ , which is an upper bound for the particles hydrogen trapping ability, by considering the particles as coherent and allowing the particles to have an arbitrary OR with the matrix. The Euler angles in the  $z - x' - z''$  convention are used to define the orientations of the local coordinates via the rotation matrix  $R$ :

$$\hat{x}_i = R_{ij}^D(\alpha^D, \beta^D, \gamma^D)\tilde{x}_j^D, \quad \hat{x}_i = R_{ij}^L(\alpha^L, \beta^L, \gamma^L)\tilde{x}_j^L, \quad (10)$$

where  $(\alpha^D, \beta^D, \gamma^D)$  and  $(\alpha^L, \beta^L, \gamma^L)$  represent the Euler angles of the local coordinates  $\tilde{x}_i^D$  and  $\tilde{x}_i^L$ , respectively. Finally, four shapes of the inclusion are investigated, including a sphere, an ellipsoid ( $a_1 : a_2 : a_3 = 5 : 4 : 3$ ), a prolate spheroid ( $a_1 : a_2 : a_3 = 5 : 1 : 1$ ), and an oblate spheroid ( $a_1 : a_2 : a_3 = 5 : 5 : 1$ ). On the inclusion surface with each shape, the minimum value of  $E_{\text{int}}$  is determined from the enumeration of both the orientation of H and the carbide by changing the Euler angles  $(\alpha^D, \beta^D, \gamma^D)$  and  $(\alpha^L, \beta^L, \gamma^L)$  at every  $2^\circ$ .

The full results of this study are included in Tables S3–S5 within the Supplemental Material [32]. The values of  $E_{\text{int}}(\text{min})$  exhibit the same trends as shown in Fig. 8 and Fig. 12. However, when the orientation is allowed to change, the magnitude of  $E_{\text{int}}(\text{min})$  increases to more than twice than that for a coherent precipitate with a fixed orientation. For the oblate spheroidal inclusion with  $a_1 : a_2 : a_3 = 5 : 5 : 1$ , the upper limits of the elastic-strain hydrogen-binding energy  $|E_{\text{int}}(\text{min})|$  for ZrC are 1.37 eV (octahedral) and 0.878 eV (tetrahedral) in  $\alpha$ -Fe as well as 0.698 eV (octahedral) and 1.04 eV (tetrahedral) in  $\gamma$ -Fe, which are the largest among the carbides with a FCC metal sublattice. The  $|E_{\text{int}}(\text{min})|$  for Nb<sub>2</sub>C are 2.34 eV (octahedral) and 1.12 eV (tetrahedral) in  $\alpha$ -Fe as well as 0.497 eV (octahedral) and 0.739 eV (tetrahedral) in  $\gamma$ -Fe, which are the largest among the carbides with a hexagonal metal sublattice. This suggests that the hydrogen-binding capability of semi-incoherent carbide precipitates could be significant, and has been noted in experiments [7, 15]. These results further indicate that the orientation of the carbide precipitate can play a significant role in governing hydrogen trapping if coherency can be maintained.

For incoherent precipitates, Wei *et al.* investigated several B1-structure based carbide precipitates (TiC, NbC, and VC) and found that those incoherent precipitates did not exhibit hydrogen-binding capability [7, 15]. These results can also be explained using the continuum model discussed in this paper. For an incoherent precipitate, the eigenstrains are small since the degree of the lattice mismatch is almost zero. Therefore, the stress and strain fields around the precipitate are negligible, which leads to trivial long-range hydrogen binding effects.

### IV. SUMMARY AND CONCLUSIONS

The main goal of this study was to estimate the ability of carbide precipitates in steels to attract hydrogen atoms to its interface due to elastic interactions. To achieve this, we used Eshelby's equivalent inclusion method to calculate the elastic interaction energy between the point defects of H and ellipsoidal shaped carbide inclusions in the iron matrix.

This paper focused on precipitates in the group VIB, VB, and VIB carbides  $\text{MC}_x$  with the stoichiometries  $0.5 \leq x \leq 1$ . Our calculations demonstrate that for coherent precipitates of the cubic carbides, hydrogen is generally attracted to the broad interface of the precipitates and is in agreement with direct experimental observations. Hydrogen is not, as previously postulated, generally attracted to the edges of the precipitates where the strain fields are the largest since the interaction is repulsive, not attractive. This is true regardless of the structure of the matrix, e.g., ferrite or austenite. The magnitude of the interaction is typically less than 0.3 eV, resulting in the elastic interaction acting as a weak trap for hydrogen. This interaction does depend on the chemistry of the cubic carbide. It is largest for the stoichiometric carbides MC because of the larger elastic constants of the carbides, which decreases with decreasing carbon content. However, we note that the transition metal also plays an important role in the magnitude of the interaction because of the lattice mismatch, which follows the trend  $\text{ZrC}_x > \text{HfC}_x > \text{TaC}_x \simeq \text{NbC}_x > \text{TiC}_x > \text{VC}_x$ . In addition, our results also suggest that hydrogen interstitials in  $\alpha$ -Fe can occupy both the octahedral and tetrahedral interstices near the broad interface of the disk-like B1-structure based carbides while the hydrogen in  $\gamma$ -Fe should occupy the octahedral interstices at these interfaces.

The carbides with the hexagonal metal sublattice also exhibit the ability to trap hydrogen at the broad coherent interface. The interaction energies are similar in magnitude to the cubic carbides, except for the octahedral interstice in  $\alpha$ -Fe, which is much larger and suggests that H might sit at the octahedral interstices near the broad interface. The magnitude of the interaction energy also changes with composition, but this change in composition is attributed to lattice mismatch instead of elastic constants, the latter of which does not drop significantly with carbon content.

To further provide evidence of the hydrogen-binding effects near the interface of carbide precipitates, we estimated the upper bound of the hydrogen-binding energy for coherent and semicoherent precipitates by enumerating the orientations of the carbides. Results indicate that semicoherent carbide precipitates have the potential to become effective hydrogen traps but strongly depends on the carbide orientations. In addition, our continuum model suggests the negligible hydrogen-binding capability for incoherent precipitates. Our findings of the hydrogen-binding capability for semicoherent and incoherent precipitates agree with the experimental observations.

Overall, results in this study indicate that the hydrogen-binding energy induced by the elastic fields depends on several factors: size, morphology, orientation, and interface character of the precipitate as well as the precipitate elastic constants and lattice mismatch, which are both a function of composition. This is further complicated by the fact that the



coherency strain changes as the particle grows, which tends to reduce the coherency strain and hence the particles hydrogen trapping ability. All these factors can impact the efficiency and effectiveness of the hydrogen binding, which may be a possible explanation for the inconsistency in experimental studies of the hydrogen trapping of NbC, VC, and Mo<sub>2</sub>C. The last point to be raised is that this paper does not include chemical factors from the local atomic configurations, which include the chemical binding of hydrogen to the interface, the formation of hydrides near dislocation cores, and the trapping of hydrogen inside carbide particles. Those factors also play important roles that can be studied with modeling approaches and has been done for stoichiometric TiC [80].

While all of the results discussed here are for ferrite and austenite, we note that they can generally be applied with little modification to ferritic and austenitic steels. Since ferritic steels typically have similar lattice constants and elastic constants to pure ferrite as studied here, our results are representative of these materials. However, as noted in the methodology, the elastic constants of austenite are about half as those of austenitic steels. Based on the elastic model, we can estimate that the elastic interaction energies here should be roughly doubled when applied to austenitic steels.

#### ACKNOWLEDGMENTS

This material is based upon work supported by the U.S. Department of Energy's Office of Energy Efficiency and Renewable Energy (EERE) under the Fuel Cell Technologies Office, Award Number DE-EE0008831. This report was prepared as an account of work sponsored by an agency of the United States Government. Neither the United States Government nor any agency thereof, nor any of their employees, makes any warranty, express or implied, or assumes any legal liability or responsibility for the accuracy, completeness, or usefulness of any information, apparatus, product, or process disclosed, or represents that its use would not infringe privately owned rights. Reference herein to any specific commercial product, process, or service by trade name, trademark, manufacturer, or otherwise does not necessarily constitute or imply its endorsement, recommendation, or favoring by the United States Government or any agency thereof. The views and opinions of authors expressed herein do not necessarily state or reflect those of the United States Government or any agency thereof.

#### APPENDIX A: NOMENCLATURE

$a_i$	≡	The semiaxes of the ellipsoidal inclusion
$\hat{x}_i$	≡	The global coordinate system along semiaxes
$C_{ijkl}^{M-iso}$	≡	The stiffness tensor of the isotropic matrix
$C_{ijkl}^M$	≡	The stiffness tensor of the anisotropic matrix
$\tilde{x}_i^D$	≡	The local coordinate system of the point defect
$R_{ij}^D$	≡	The rotation matrix for $\tilde{x}_i^D$ : $\hat{x}_i = R_{ij}^D \tilde{x}_j^D$

$\tilde{P}_{ij}$	≡	The elastic dipole tensor in the local coordinate system $\tilde{x}_i^D$
$P_{ij}$	≡	The elastic dipole tensor in the global coordinate system $\hat{x}_i$
$\tilde{x}_i^l$	≡	The local coordinate system of the inclusion
$R_{ij}^l$	≡	The rotation matrix for $\tilde{x}_i^l$ : $\hat{x}_i = R_{ij}^l \tilde{x}_j^l$
$\tilde{C}_{ijkl}^l$	≡	The stiffness tensor of the anisotropic inclusion in the local coordinate system $\tilde{x}_i^l$
$C_{ijkl}^l$	≡	The stiffness tensor of the anisotropic inclusion in the global coordinate system $\hat{x}_i$
$\tilde{\varepsilon}_{ij}^{l*}$	≡	The eigenstrain of the inclusion in the local coordinate system $\tilde{x}_i^l$
$\varepsilon_{ij}^{l*}$	≡	The eigenstrain of the inclusion in the global coordinate system $\hat{x}_i$
$\varepsilon_{ij}^*$	≡	The equivalent eigenstrain of the inclusion in the global coordinate system $\hat{x}_i$
$D_{ijkl}^{in}$	≡	The Eshelby tensor inside the inclusion
$D_{ijkl}^{out}$	≡	The Eshelby tensor outside the inclusion
$\varepsilon_{ij}^c$	≡	The constraint strain in the global coordinate system $\hat{x}_i$
$E_{int}$	≡	The elastic-strain interaction energy between the point defect and the inclusion
$E_o$	≡	The ground-state energy of a Fe supercell with an octahedral interstice H
$E_t$	≡	The ground-state energy of a Fe supercell with an octahedral interstice H
$\Delta E_{ot}$	≡	The energy difference between H at different types of interstices.

#### APPENDIX B: QUANTITATIVE ANALYSES OF THE APPROXIMATIONS IN THE CONTINUUM MODEL

##### 1. The isotropic and anisotropic elasticity of the Fe matrix

In our simulations, we chose to implement Eshelby's solution using isotropic elasticity for the iron matrix. However, it is clear that the elastic constants of the matrix, either ferrite and austenite, are anisotropic. The use of the isotropic approximation for the matrix might appear at first an unusual choice, but there are several reasons to make this choice. The first is the expediency of the solution. The assumption of isotropy results in closed forms for the Eshelby tensor  $D_{ijkl}^{out}$  [24,25,31], which makes the evaluation of the interaction energy expeditious; anisotropy would require the use of surface integrals or Fourier transforms to evaluate the Eshelby tensor. This allows us to more thoroughly evaluate how different structural features affect the interaction energy. Another rationale to use isotropy is that it makes extension of our results relatively straightforward. For example, it is straightforward to extrapolate our results for pure austenite to austenitic stainless steels by scaling with the Young's modulus. To sum up, using simple isotropic elastic constants that can be scale is less accurate for pure iron, but much more useful in understanding how our results would scale to steel.

To demonstrate that using isotropic elasticity of the Fe matrix (as well as other approximations made in our model) does not create large errors, we compare the calculated  $E_{int}$  in the present study with the reported data from DFT simulation [80]. Di Stefano *et al.* modeled the interface between TiC

TABLE III. The computed minimum elastic interaction energy  $E_{\text{int}}(\text{min})$  between a H atom and the ellipsoidal TiC particle with  $a_1 : a_2 : a_3 = 5 : 5 : 1$ . Different data of the lattice constant and the elastic constant for the Fe matrix are used. The Baker-Nutting orientation relation is chosen where the coherent interface normal is  $[100]_{\alpha} \parallel [100]_{\text{TiC}}$ . In the table,  $a_0$  represents the lattice constant,  $K$  represents the bulk modulus and  $\nu$  stands for the Poisson's ratio.

Matrix	Methods	$a_0$ (Å)	$K$ (GPa)	$\nu$	Nonzero $\varepsilon_{ij}^{I*}$ $\varepsilon_{22}^{I*} = \varepsilon_{33}^{I*} \neq 0$	$E_{\text{int}}(\text{min})$ at $(0, 0, a_3)$ (eV)	
						Octahedral H	Tetrahedral H
$\alpha$ -Fe	DFT at 0 K	2.832	187	0.302	0.08288	-0.180	-0.110
	DFT+DG at 300 K	2.849	161	0.302	0.7642	-0.156	-0.0958
	Exp. at 300 K <sup>a</sup>	2.862	157	0.287	0.07153	-0.140	-0.0886
$\gamma$ -Fe	DFT at 0 K	3.477	183	0.191	0.2474	-0.171	-0.255
	DFT+DG at 1428 K	3.509	130	0.191	0.2360	-0.149	-0.221
	Exp. at 1428 K <sup>b</sup>	3.613	126	0.360	0.2003	-0.0810	-0.120

<sup>a</sup>Reference [37,38].

<sup>b</sup>Reference [36].

and  $\alpha$ -Fe as an infinite plane and reported the elastic-strain contribution to the H binding energy as  $-0.18$  eV for H atoms at the tetrahedral interstice. In their DFT simulations, the anisotropy of the matrix was fully considered. Using the continuum model, we computed  $E_{\text{int}}$  for a spherical TiC inclusion since the infinite plane can be viewed as a sphere with an infinite radius. We found values of  $E_{\text{int}}(\text{min})$  of  $-0.192$  eV for tetrahedral-interstitial H at the position P1 and  $-0.153$  eV for H at the position P2/P3. These values obtained in our continuum model are in good agreement with the reported data in DFT simulation, which demonstrates that the approximations and simplifications in our model are valid and do not produce large errors.

## 2. The lattice constant and elastic constant of the Fe matrix obtained in different approaches

As stated in Sec. III, we chose to use the experimental values of the lattice constant and elastic constant for the Fe matrix in Eq. (6) to compute  $E_{\text{int}}$ . The rationale for this is that the real interest here is in understanding hydrogen trapping in austenitic and ferritic steels, not pure Fe. Pure ferrite, as noted in the text, is generally a good substitute for ferritic steels as the addition of carbon and alloying elements typically do not change the structure or elastic constants appreciably. In austenite, the lattice constants are similar to austenitic stainless steels but the elastic constants are different. Thus, in this manuscript we used the experimental model of austenite and discussed how the answers might change if the material selected is an austenitic steel. However, our results do use the experimental values instead of DFT values and it is important to understand if this creates substantial inconsistencies because we use DFT data for the carbides.

To complete this comparison, we evaluated the lattice constants and elastic constants of ferrite and austenite in DFT at conditions comparable to those in experiments, which are ferrite at room temperature and austenite at 1428 K. To evaluate the lattice constant and elastic constant of Fe at a finite temperature based on DFT simulations, the Debye-Grüneisen model (DG model) was used [81]. We performed the DFT calculations for  $\alpha$ -Fe and  $\gamma$ -Fe with different volumes by using the parameters in Sec. II C. Then that data was fitted to a Morse-potential  $E_{DFT}(V)$  and the Debye frequency  $\theta_D$  was

calculated from  $\partial E_{DFT}(V)/\partial V$  and  $\partial^2 E_{DFT}(V)/\partial V^2$ . Next, the internal energy  $E_D(T, V)$  and the entropy  $S_D(T, V)$  of phonons were computed by using  $\theta_D$ . By minimizing the Helmholtz free energy  $F(T, V)$  in Eq. (B1), the equation of state  $V(T)$  was determined:

$$F(T, V) = E_{DFT}(V) + E_D(T, V) - TS_D(T, V) + E_{el}(T, V) - TS_{el}(T, V). \quad (\text{B1})$$

In Eq. (B1), the term  $E_{el}(T, V)$  and  $S_{el}(T, V)$  stands for the heat-excited electronic internal energy and enthalpy, respectively, which can be evaluated using the DOSCAR from DFT simulations. Results of the lattice constant and heat capacity of Fe obtained from DFT calculations at finite temperatures are plotted in Fig. 14.

These results suggest that both the lattice constant and heat capacity of  $\alpha$ -Fe obtained from the DFT calculation are consistent with the experimental data. However, while the heat capacity of  $\gamma$ -Fe obtained from the DFT calculation agrees with the experimental data, the lattice constant is off by about 3%. This indicates the DFT calculation can correctly model

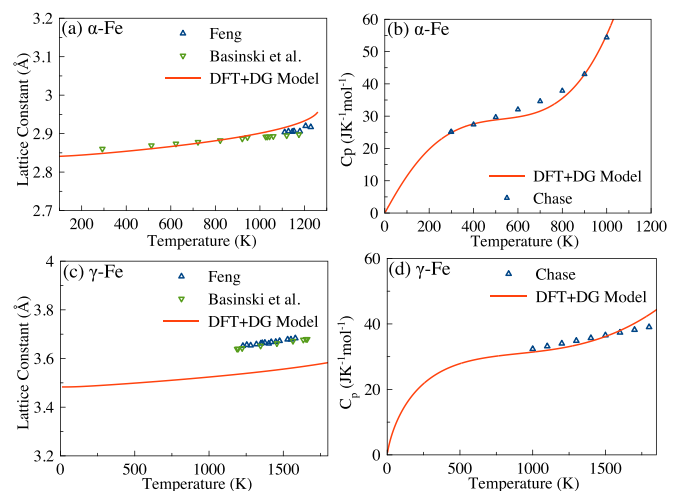


FIG. 14. The calculated lattice constant and heat capacity using the Debye-Grüneisen model compared with the experimental data. Experimental data of the lattice constant for (a)  $\alpha$ -Fe and (c)  $\gamma$ -Fe: Feng [82], Basinski *et al.* [83]. Experimental data of the heat capacity of (b)  $\alpha$ -Fe and (d)  $\gamma$ -Fe: Chase [84].

the bulk modulus of  $\gamma$ -Fe, while there is some error in evaluating the lattice constant. Using this new data for the matrix, we computed the  $E_{\text{int}}(\text{min})$  between a H atom and the oblate spheroidal TiC particle at  $(0, 0, a_3)$ . These results are listed in Table III.

Results indicate that for  $\alpha$ -Fe, the values of  $E_{\text{int}}(\text{min})$  do not change significantly when different material-specific data were used in the model (experiments vs DFT) because the DFT calculations show good agreement with experiments in both the lattice constant and elastic constant. However, the significant discrepancy exists in  $E_{\text{int}}(\text{min})$  for  $\gamma$ -Fe even though the computed bulk modulus at 1428 K is close to the experimental value. This difference in  $E_{\text{int}}(\text{min})$  is attributed to the eigenstrain of the inclusion and the Young's modulus of the matrix, which can be seen from Eq. (6). Therefore, to make the results meaningful for  $\gamma$ -Fe, we chose experimental data of  $\gamma$ -Fe measured at 1428 K in this paper since it is a more accurate representation of both austenite and austenitic stainless steels. Finally, it is worth noting that if we use the DFT data for the Fe matrix, the scaling of  $E_{\text{int}}(\text{min})$  is nearly the same for the carbides with similar structures (fcc metal sublattice or hexagonal metal sublattice). This means that the trends of  $E_{\text{int}}(\text{min})$  amongst the carbides found in this study are still valid.

### 3. The H-H interaction

As mentioned in Sec. II A, a simplified two-body continuum model was employed that neglects long-range H-H interaction. In general, there are two different types of the H-H interaction: one is the aggregation of H atoms, which leads to the formation of hydrides, and the other is the long-range elastic H-H interaction. The formation of hydrides depends on the local hydrogen arrangement, which cannot be investigated in this continuum model since we did not choose to evaluate the energy of aggregated hydrogen atoms and is beyond the scope of this paper, which is to evaluate the individual interactions between atomic hydrogen and carbide particles.

However, the long-range elastic H-H interactions can be estimated using the anisotropic elasticity toolkit (ANETO) [72]. As discussed in Sec. II C, DFT calculations were performed for different Fe supercells with one H interstitial. Due to the periodic boundary conditions in DFT simulations, the H atom (point defect) inside the Fe matrix with  $N$  atomic sites has the elastic interaction  $\Delta E_{H-H}$  with its image atoms. This energy  $\Delta E_{H-H}$  can be approximated as the average long-range elastic H-H interactions inside the bulk Fe with  $1/N$  composition of hydrogen. The computed results using ANETO are illustrated in Fig. 15.

These results suggest that the choice of two-body model is valid for two reasons. First, the elastic long-range interaction between H interstitials are repulsive since the H atom (point defects) generally produce dilatational stress-strain fields. Second, the concentration of H atoms inside iron/steels is small in practical cases. In references [85–87], the threshold concentrations of hydrogen were determined experimentally based on the initiation of cracks. Experimental results suggest that, when the ultimate tensile stress (UTS) of ferritic/martensitic steels is about 1 GPa, the threshold concentration of hydrogen is 0.5 – 8.5 wt ppm, which is  $2.8 \times 10^{-5} - 4.7 \times 10^{-4}$  molar fraction. This threshold con-

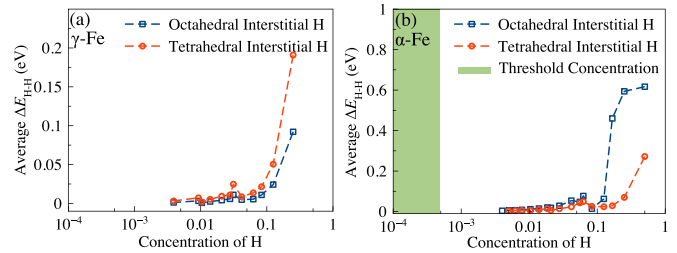


FIG. 15. (a) The computed average elastic long-range interaction between H atoms inside  $\gamma$ -Fe via DFT simulations; (b) The computed average elastic long-range interaction between H atoms inside  $\alpha$ -Fe via DFT simulations. The light green region in the subplot (b) represents the threshold concentration of hydrogen in ferritic/martensitic steels with its ultimate tensile stress (UTS) is 1 GPa.

centration range is labeled in Fig. 15(b) and obviously the average  $\Delta E_{H-H}$  is negligible ( $< 10^{-4}$  eV).

### 4. The shape effect between a cylindrical inclusion and an ellipsoidal inclusion

The growth of secondary-phase particles, including transition metal carbides, are governed by both the surface energy and the volumetric elastic energy as discussed above. For small coherent precipitates, the precipitates typically form a flat platelet where the broad surface has the minimum surface energy. As the precipitate grows, the volumetric elastic energy gradually dominates over the surface energy by changing the shape of the precipitate, and thus the ellipsoidal or spherical particles are observed for semicoherent and incoherent precipitates. This typical growth pattern of precipitates is discussed within the Supplemental Material [32], which is also confirmed in many experimental observations. Wei *et al.* approximated the small coherent precipitates as flat discs based on the TEM images (Fig. 2 in Ref. [7]). Takahashi *et al.* conducted the direct observation of coherent TiC precipitates using APT and also suggested that the particles were flat platelets/disks [16]. For the semicoherent and incoherent precipitates, the ellipsoidal or spherical shapes were observed in experiments [7,88]. In order to implement the Eshelby's solution, the coherent precipitates are modeled as oblate spheroids in the present study instead of the disk/cylinder shapes for numerical convenience. While experiments cannot truly resolve if the precipitates are truly cylindrical discs or oblate spheroids, it is important to establish how each of these models impact the results as that has an impact on the error in our model.

Unlike an ellipsoidal inclusion, the Eshelby tensor of a cylindrical inclusion does not have an explicit form. Moreover, the simple linear relationship between the constraint strain  $\varepsilon^c$  and the eigenstrain  $\varepsilon^*$  does not exist in cylindrical inclusions. Using the Green's function and Fourier transform, thus the constraint strain has to be computed using Eqs. (B2) and (B3):

$$G_{ij}(\vec{x}) = \left(\frac{1}{2\pi}\right)^3 \int_{-\infty}^{\infty} \frac{\exp(-i\vec{k} \cdot \vec{x})}{k^2} \left[ \frac{C_{imjn}^M k_m k_n}{k^2} \right]^{-1} d\vec{k}, \quad (\text{B2})$$

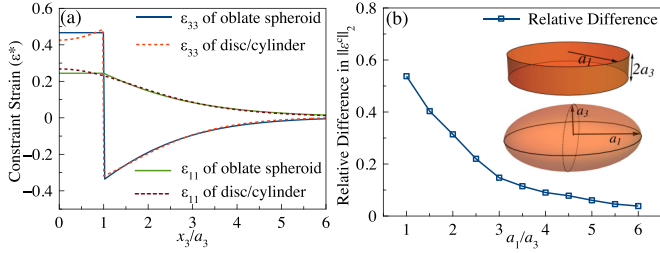


FIG. 16. (a) The constraint strain  $\epsilon_{ij}^c$  along the  $\hat{x}_3$  axis of the cylindrical inclusion and the ellipsoidal inclusion. The shape is chosen as  $a_1 : a_2 : a_3 = 5 : 5 : 1$  and the eigenstrain is set isotropic on the  $\hat{x}_1\hat{x}_2$  plane as  $\epsilon_{11}^* = \epsilon_{22}^* = \epsilon^*$ . The constraint strain  $\epsilon_{ij}^c$  is scaled with respect to  $\epsilon^*$  (b) The relative difference in the constraint strain  $\epsilon^c$  at  $(0, 0, a_3)$  between the cylindrical and ellipsoidal inclusions.

$$\epsilon_{ij}^c(\vec{x}) = -\frac{1}{2} \oint C_{pqrs}^M \epsilon_{rs}^* n_q(\vec{x}') \times [G_{im,j}(\vec{x} - \vec{x}') + G_{jm,i}(\vec{x} - \vec{x}')] dS(\vec{x}'), \quad (\text{B3})$$

To compare  $\epsilon^c$  between the two different shapes of the inclusion, the radius and the height of the cylindrical inclusion, labeled as  $a_1$  and  $a_3$ , are  $a_1 : a_3 = 5$  and for the oblate spheroid:  $a_1 : a_2 : a_3 = 5 : 5 : 1$ . The eigenstrain is set to be isotropic on  $\hat{x}_1 - \hat{x}_2$  plane as  $\epsilon_{11}^* = \epsilon_{22}^* = \epsilon^*$ . The components of the constraint strain  $\epsilon_{ij}^c$  along the  $\hat{x}_3$  axis are plotted in Fig. 16(a). A slight difference in  $\epsilon^c$  is found inside the inclusion and near the inclusion boundary. At the point  $(0, 0, a_3)$ , which associated with the largest elastic H binding energy, the relative difference in the constraint strain is computed in Eq. (B4):

$$\eta = \frac{2\|\epsilon^c(\text{disc}) - \epsilon^c(\text{oblate})\|_2}{\|\epsilon^c(\text{disc})\|_2 + \|\epsilon^c(\text{oblate})\|_2}, \quad (\text{B4})$$

where  $\|\epsilon^c\|$  stands for the norm 2 of the constraint strain. Figure 16(b) shows that for flat platelets  $a_1/a_3 > 3$ , the relative difference in the shape effect between the disk and oblate spheroid is less than 10%. In this study, we chose the shape of coherent precipitates as the oblate spheroid with  $a_1 : a_3 = 5$ , which may cause about 7% relative difference compared to a disk shaped inclusion.

Therefore, choosing the ellipsoidal inclusion instead of the cylindrical inclusion would bring about 7% relative difference, which would not change the conclusion in this study. However, modeling the inclusion as an ellipsoid dramatically lowers the computational effort. Furthermore, it is worth returning to the point that we do not know the true shape of the precipitate: is it a disk or an oblate spheroid? This paper clearly demonstrates that for platelet shapes, the difference is small and thus both models will give similar answers and, for more equiaxed shapes that occur as the precipitates grow, the ellipsoidal model is much more appropriate than a cylinder as the experimental shapes agree much more with ellipsoids than cylinders.

### 5. The magnetostrictive effect inside $\alpha$ -Fe

The magnetostriction in  $\alpha$ -Fe has the potential to create a magnetostrictive strain and thus contribute to the elastic

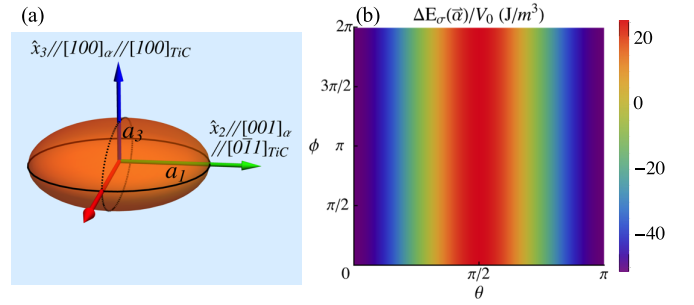


FIG. 17. (a) The oblate spheroidal TiC particle inside  $\alpha$ -Fe, where  $a_1 : a_2 : a_3 = 5 : 5 : 1$  and the Baker-Nutting orientation relation is adopted. (b) The magneto-elastic energy  $\Delta E_{\sigma}(\vec{\alpha})$  caused by the stress field around the TiC particle with respect to the magnetization orientation  $\vec{\alpha}(\theta, \phi)$ .

interaction energy  $E_{\text{int}}$  between H atoms and carbides. In a continuum model, the first-order linear term in the magnetostriction is zero because no external magnetic field is applied on the bcc  $\alpha$ -Fe (and  $\alpha$ -Fe is centrosymmetric). Therefore, we assume the change in  $E_{\text{int}}$  is negligible due to the magnetostriction. However, below we will quantify this and demonstrate the effects can be neglected.

If we consider magnetostriction in the continuum model, the stress-strain field around the carbide particle is coupled with the internal magnetization  $\vec{M}(\vec{\alpha})$  where  $\vec{\alpha} = (\alpha_1, \alpha_2, \alpha_3)$  is the magnetization orientation. The internal energy change due to the magnetization is therefore [89]:

$$\Delta E(\vec{\alpha}) = \Delta E_m(\vec{\alpha}) + \Delta E_{\sigma}(\vec{\alpha}), \quad (\text{B5})$$

$$\Delta E_m(\vec{\alpha}) = K_1(\alpha_1^2\alpha_2^2 + \alpha_2^2\alpha_3^2 + \alpha_1^2\alpha_3^2) + K_2\alpha_1^2\alpha_2^2\alpha_3^2, \quad (\text{B6})$$

where  $\Delta E_m(\vec{\alpha})$  is the anisotropic magnetization energy and  $\Delta E_{\sigma}(\vec{\alpha})$  is the magneto-elastic energy. The term  $\Delta E_{\sigma}(\vec{\alpha})$  is computed as the tensor contraction between the stress  $\sigma_{ij}$  and the magnetostriction strain  $\epsilon_{ij}^{\mu}(\vec{\alpha})$ :

$$\Delta E_{\sigma}(\vec{\alpha}) = -\sigma_{ij}\epsilon_{ij}^{\mu}(\vec{\alpha}). \quad (\text{B7})$$

The magnetostriction strain  $\epsilon_{ij}^{\mu}(\vec{\alpha})$  for a single crystal  $\alpha$ -Fe is defined in Eq. (B8):

$$\epsilon_{ij}^{\mu}(\vec{\alpha}) = \frac{3}{2} \begin{bmatrix} \lambda_{100}(\alpha_1^2 - \frac{1}{3}) & \lambda_{111}\alpha_1\alpha_2 & \lambda_{111}\alpha_1\alpha_3 \\ \lambda_{111}\alpha_2\alpha_1 & \lambda_{100}(\alpha_2^2 - \frac{1}{3}) & \lambda_{111}\alpha_2\alpha_3 \\ \lambda_{111}\alpha_3\alpha_1 & \lambda_{111}\alpha_3\alpha_2 & \lambda_{100}(\alpha_3^2 - \frac{1}{3}) \end{bmatrix}. \quad (\text{B8})$$

In Eq. (B8),  $\lambda_{100}$  and  $\lambda_{111}$  represent the magnetostriction constants along  $\langle 100 \rangle_{\alpha}$  and  $\langle 111 \rangle_{\alpha}$ , which are temperature dependent. At 300 K,  $\lambda_{100} = 2.2 \times 10^{-5}$ ,  $\lambda_{111} = -1.7 \times 10^{-5}$ ,  $K_1 = 4.8 \times 10^4 \text{ J/m}^3$ , and  $K_2 = 1.5 \times 10^4 \text{ J/m}^3$  [90]. The magnetization orientation  $\vec{\alpha}$  can be determined by minimizing  $\Delta E(\vec{\alpha})$  in Eq. (B5).  $\Delta E_m(\vec{\alpha})$  has a minimum value when  $\vec{\alpha} \parallel \langle 100 \rangle_{\alpha}$ , which means the magnetization of a single crystal  $\alpha$ -Fe without internal stresses prefers  $\langle 100 \rangle_{\alpha}$  directions. To evaluate  $\Delta E_{\sigma}(\vec{\alpha})$  in our model, we use a coherent TiC precipitate as an example with the Baker-Nutting orientation. The Baker-Nutting orientation relation was implemented by choosing the normal vector of the coherent interfaces as  $\hat{x}_3 \parallel$



TABLE IV. The contribution of the magnetostriction in the elastic interaction between H atoms and TiC particle inside  $\alpha$ -Fe, noted as  $\Delta E_{\text{int}}^{\mu}(\vec{\alpha})$  with units in eV. The magnetization orientation is determined to be parallel to the normal vector of the coherent interfaces:  $\vec{\alpha} \parallel [100]_{\alpha} \parallel [100]_{\text{TiC}}$ .

	Octahedral interstitial		Tetrahedral interstitial	
	P1	P2/P3	P1	P2/P3
$\Delta E_{\text{int}}^{\mu}(\vec{\alpha})$	$-7.11 \times 10^{-5}$	$3.55 \times 10^{-5}$	$8.14 \times 10^{-6}$	$-4.07 \times 10^{-6}$

$[100]_{\alpha} \parallel [100]_{\text{TiC}}$ . The TiC particle was modeled as an oblate spheroidal inclusion with the semiaxes  $a_1 : a_2 : a_3 = 5 : 5 : 1$ .

The orientation of  $\vec{\alpha}$  is defined by the polar angle ( $\theta$ ) and the azimuthal angle ( $\phi$ ) in the global coordinate system  $\hat{x}_i$  as illustrated in Fig. 17(a). The volume integral of  $\Delta E_{\sigma}(\vec{\alpha})$  was then performed in the ellipsoidal region  $\lambda a_i$  with  $\lambda \in [1, 30]$ ,

and the minimum value of  $\Delta E_{\sigma}(\vec{\alpha})$  was found when  $\vec{\alpha} \parallel \hat{x}_3 \parallel [100]_{\alpha} \parallel [100]_{\text{TiC}}$  ( $\theta = 0$ ).

As illustrated in Fig. 17(a), although large internal stresses exist on the  $(100)_{\alpha}$  plane near the edge of the TiC platelet due to the lattice mismatch, this stress field is compressive and thus unfavorable for the magnetization. Taking both  $\Delta E_m(\vec{\alpha})$  and  $\Delta E_{\sigma}(\vec{\alpha})$  into consideration, the magnetization orientation  $\vec{\alpha}$  is along the normal vector of the coherent interfaces  $[100]_{\alpha} \parallel [100]_{\text{TiC}}$ . The correction term due to the magnetostriction in the elastic interaction  $E_{\text{int}}$  is computed afterwards as

$$\Delta E_{\text{int}}^{\mu}(\vec{\alpha}) = -P_{ij}\epsilon_{ij}^{\mu}(\vec{\alpha}), \quad (\text{B9})$$

where  $P_{ij}$  is the elastic dipole tensor of an interstitial H. As listed in Table IV, values of  $\Delta E_{\text{int}}^{\mu}(\vec{\alpha})$  are in the magnitude of  $10^{-6} - 10^{-5}$  eV, which justifies the assumption that the magnetostriction is negligible in our model.

- 
- [1] G. M. Pressouyre and I. M. Bernstein, *Acta Metall.* **27**, 89 (1979).
- [2] S. Yamasaki and T. Takahashi, *Tetsu-to-Hagane* **83**, 454 (1997).
- [3] S. Zhang, Y. Huang, B. Sun, Q. Liao, H. Lu, B. Jian, H. Mohrbacher, W. Zhang, A. Guo, and Y. Zhang, *Mater. Sci. Eng., A* **626**, 136 (2015).
- [4] T. Depover and K. Verbeken, *Int. J. Hydrogen Energy* **41**, 14310 (2016).
- [5] F. G. Wei, T. Hara, and K. Tsuzaki, *Philos. Mag.* **84**, 1735 (2004).
- [6] T. Baker, *Mater. Sci. Technol.* **25**, 1083 (2009).
- [7] F. G. Wei, T. Hara, and K. Tsuzaki, in *Advanced Steels*, edited by Y. Weng, H. Dong, and Y. Gan (Springer, Berlin, 2011), pp. 87–92.
- [8] T. Asaoka, G. Lapasset, M. Aucouturier, and P. Lacombe, *Corrosion* **34**, 39 (1978).
- [9] G. M. Pressouyre and I. M. Bernstein, *Metall. Trans. A* **9**, 1571 (1978).
- [10] G. M. Pressouyre and I. M. Bernstein, *Metall. Trans. A* **12**, 835 (1981).
- [11] H. Lee and J. Y. Lee, *Acta Metall.* **32**, 131 (1984).
- [12] S. M. Lee and J. Y. Lee, *Acta Metall.* **35**, 2695 (1987).
- [13] F.-G. Wei, T. Hara, T. Tsuchida, and K. Tsuzaki, *ISIJ International* **43**, 539 (2003).
- [14] F. G. Wei, T. Hara, and K. Tsuzaki, *Metall. Mater. Trans. B* **35**, 587 (2004).
- [15] F. G. Wei and K. Tsuzaki, *Metall. Mater. Trans. A* **37**, 331 (2006).
- [16] J. Takahashi, K. Kawakami, Y. Kobayashi, and T. Tarui, *Scr. Mater.* **63**, 261 (2010).
- [17] J. Takahashi, K. Kawakami, and T. Tarui, *Scr. Mater.* **67**, 213 (2012).
- [18] J. Takahashi, K. Kawakami, and Y. Kobayashi, *Acta Mater.* **153**, 193 (2018).
- [19] Y.-S. Chen, D. Haley, S. S. A. Gerstl, A. J. London, F. Sweeney, R. A. Wepf, W. M. Rainforth, P. A. J. Bagot, and M. P. Moody, *Science* **355**, 1196 (2017).
- [20] Y.-S. Chen, H. Lu, J. Liang, A. Rosenthal, H. Liu, G. Sneddon, I. McCarroll, Z. Zhao, W. Li, A. Guo, and J. M. Cairney, *Science* **367**, 171 (2020).
- [21] M. Ohnuma, J. ichi Suzuki, F.-G. Wei, and K. Tsuzaki, *Scr. Mater.* **58**, 142 (2008).
- [22] F. Wei and K. Tsuzaki, in *Gaseous Hydrogen Embrittlement of Materials in Energy Technologies*, Woodhead Publishing Series in Metals and Surface Engineering, Vol. 2, edited by R. P. Gangloff and B. P. Somerday (Woodhead Publishing, Cambridge, 2012), pp. 493–525.
- [23] J. Lee, T. Lee, Y. J. Kwon, D.-J. Mun, J.-Y. Yoo, and C. S. Lee, *Corros. Rev.* **33**, 433 (2015).
- [24] J. D. Eshelby and R. E. Peierls, *Proc. R. Soc. London A* **241**, 376 (1957).
- [25] J. D. Eshelby and R. E. Peierls, *Proc. R. Soc. London A* **252**, 561 (1959).
- [26] I. M. Robertson, P. Sofronis, A. Nagao, M. L. Martin, S. Wang, D. W. Gross, and K. E. Nygren, *Metall. Mater. Trans. A* **46**, 2323 (2015).
- [27] R. Gangloff and B. Somerday, *Gaseous Hydrogen Embrittlement of Materials in Energy Technologies: The Problem, its Characterisation and Effects on Particular Alloy Classes*, Woodhead Publishing Series in Metals and Surface Engineering (Elsevier Science, Cambridge, 2012).
- [28] W. Cai, W. Nix, and M. R. Society, *Imperfections in Crystalline Solids*, MRS-Cambridge Materials Fundamentals (Cambridge University Press, Cambridge, 2016), Chap. 4, pp. 71–96.
- [29] E. Clouet, C. Varvenne, and T. Jourdan, *Comput. Mater. Sci.* **147**, 49 (2018).
- [30] T. Mura, *Micromechanics of Defects in Solids*, Mechanics of Elastic and Inelastic Solids (Kluwer Academic Publishers, Dordrecht, 1987), Chap. 3, pp. 129–161.
- [31] X. Jin, D. Lyu, X. Zhang, Q. Zhou, Q. Wang, and L. Keer, *J. Appl. Mech.* **83**, 121010 (2016).
- [32] See Supplemental Material at <http://link.aps.org/supplemental/10.1103/PhysRevMaterials.5.103603> for (1) the discussion of the standard growth pattern of the secondary-phase carbides

- in iron/steel; (2) the input data for the continuum model in this paper obtained from DFT calculations the lattice constants, elastic constants, and eigenstrains of carbides; (3) the collective results of the maximum long-range hydrogen-binding energy at the carbide interfaces in iron.
- [33] D. Sholl and J. Steckel, *Density Functional Theory: A Practical Introduction* (Wiley, Hoboken, NJ, 2011).
- [34] Fe crystal structure: Datasheet from PAULING FILE Multinaries Edition-2012 in SpringerMaterials [https://materials.springer.com/isp/crystallographic/docs/sd\\_0375087](https://materials.springer.com/isp/crystallographic/docs/sd_0375087), (2016).
- [35] Fe crystal structure: Datasheet from PAULING FILE Multinaries Edition-2012 in SpringerMaterials [https://materials.springer.com/isp/crystallographic/docs/sd\\_0454654](https://materials.springer.com/isp/crystallographic/docs/sd_0454654), (2016).
- [36] J. Zarestky and C. Stassis, *Phys. Rev. B* **35**, 4500 (1987).
- [37] S. K. Satija, R. P. Comès, and G. Shirane, *Phys. Rev. B* **32**, 3309 (1985).
- [38] J. J. Adams, D. S. Agosta, R. G. Leisure, and H. Ledbetter, *J. Appl. Phys.* **100**, 113530 (2006).
- [39] A. Teklu, H. Ledbetter, S. Kim, L. A. Boatner, M. McGuire, and V. Keppens, *Metall. Mater. Trans. A* **35**, 3149 (2004).
- [40] S. A. Kim and W. L. Johnson, *Mater. Sci. Eng., A* **452-453**, 633 (2007).
- [41] D. H. Chung and W. R. Buessem, *J. Appl. Phys.* **39**, 2777 (1968).
- [42] J. M. J. den Toonder, J. A. W. van Dommelen, and F. P. T. Baaijens, *Modell. Simul. Mater. Sci. Eng.* **7**, 909 (1999).
- [43] A. Gusev, A. Rempel, and A. Magerl, *Disorder and Order in Strongly Nonstoichiometric Compounds: Transition Metal Carbides, Nitrides and Oxides*, Springer Series in Materials Science (Springer-Verlag, Berlin, 2001), Chap. 8, pp. 299–331.
- [44] X.-X. Yu, C. R. Weinberger, and G. B. Thompson, *Comput. Mater. Sci.* **112**, 318 (2016).
- [45] C. Xie, A. R. Oganov, D. Li, T. T. Debela, N. Liu, D. Dong, and Q. Zeng, *Phys. Chem. Chem. Phys.* **18**, 12299 (2016).
- [46] V. N. Lipatnikov, L. V. Zueva, A. I. Gusev, and A. Kottar, *Phys. Solid State* **40**, 1211 (1998).
- [47] V. N. Lipatnikov, A. Kottar, L. V. Zueva, and A. I. Gusev, *Inorg. Mater.* **36**, 155 (2000).
- [48] K. Yvon and E. Parthé, *Acta Crystallogr. Sect. B* **26**, 149 (1970).
- [49] E. Parthé and K. Yvon, *Acta Crystallogr. Sect. B* **26**, 153 (1970).
- [50] C. R. Weinberger, H. Yu, B. Wang, and G. B. Thompson, *Adv. Appl. Ceram.* **117**, s26 (2018).
- [51] C. R. Weinberger and G. B. Thompson, *Acta Crystallogr. Sect. B* **75**, 870 (2019).
- [52] C. R. Weinberger and G. B. Thompson, *J. Am. Ceram. Soc.* **101**, 4401 (2018).
- [53] M. de Jong, W. Chen, T. Angsten, A. Jain, R. Notestine, A. Gamst, M. Sluiter, C. Krishna Ande, S. van der Zwaag, J. J. Plata *et al.*, *Sci. Data* **2**, 150009 (2015).
- [54] D. Connétable, *Mater. Res. Express* **3**, 126502 (2016).
- [55] H. Goretzki, *Phys. Status Solidi B* **20**, K141 (1967).
- [56] V. Moisy-Maurice, N. Lorenzelli, C. De Novion, and P. Convert, *Acta Metall.* **30**, 1769 (1982).
- [57] A. L. Bowman, T. C. Wallace, J. L. Yarnell, R. G. Wenzel, and E. K. Storms, *Acta Crystallogr.* **19**, 6 (1965).
- [58] E. Rudy and C. E. Brukl, *J. Am. Ceram. Soc.* **50**, 265 (1967).
- [59] T. Epicier and P. Convert, *Phys. B: Condens. Matter* **156-157**, 41 (1989).
- [60] F. Vogel, S. Ngai, C. Smith, R. Holler, C. Weinberger, N. Wanderka, and G. Thompson, *Micron* **122**, 32 (2019).
- [61] P. E. Blöchl, *Phys. Rev. B* **50**, 17953 (1994).
- [62] G. Kresse and D. Joubert, *Phys. Rev. B* **59**, 1758 (1999).
- [63] J. P. Perdew, K. Burke, and M. Ernzerhof, *Phys. Rev. Lett.* **77**, 3865 (1996).
- [64] J. P. Perdew, J. A. Chevary, S. H. Vosko, K. A. Jackson, M. R. Pederson, D. J. Singh, and C. Fiolhais, *Phys. Rev. B* **46**, 6671 (1992).
- [65] Z. Chen, N. Kioussis, N. Ghoniem, and D. Seif, *Phys. Rev. B* **81**, 094102 (2010).
- [66] M. J. Gillan, *Philos. Mag. A* **43**, 301 (1981).
- [67] M. J. Gillan, *Philos. Mag. A* **48**, 903 (1983).
- [68] G. Simonelli, R. Pasianot, and E. J. Savino, *Phys. Rev. B* **50**, 727 (1994).
- [69] C. Varvenne and E. Clouet, *Phys. Rev. B* **96**, 224103 (2017).
- [70] R. Nazarov, J. S. Majevadia, M. Patel, M. R. Wenman, D. S. Balint, J. Neugebauer, and A. P. Sutton, *Phys. Rev. B* **94**, 241112(R) (2016).
- [71] S. MacEwen, C. Coleman, C. Ells, and J. Faber, *Acta Metall.* **33**, 753 (1985).
- [72] C. Varvenne, F. Bruneval, M.-C. Marinica, and E. Clouet, *Phys. Rev. B* **88**, 134102 (2013).
- [73] D. E. Jiang and E. A. Carter, *Phys. Rev. B* **70**, 064102 (2004).
- [74] A. Davenport, L. Brossard, and R. Miner, *JOM* **27**, 21 (1975).
- [75] W. Pitsch and A. Schrader, *Archiv für das Eisenhüttenwesen* **29**, 485 (1958).
- [76] W. Burgers, *Physica* **1**, 561 (1934).
- [77] D. Potter, *J. Less-Common Met.* **31**, 299 (1973).
- [78] W. Rong and G. Dunlop, *Acta Metall.* **32**, 1591 (1984).
- [79] D. Porter and K. Easterling, *Phase Transformations in Metals and Alloys (Revised Reprint)* (CRC Press, Boca Raton, FL, 2009), Chap. 5, pp. 261–381.
- [80] D. Di Stefano, R. Nazarov, T. Hickel, J. Neugebauer, M. Mrovec, and C. Elsässer, *Phys. Rev. B* **93**, 184108 (2016).
- [81] X.-G. Lu, M. Selleby, and B. Sundman, *Acta Mater.* **53**, 2259 (2005).
- [82] Z. Feng, The Lattice Parameter of Gamma Iron and Iron-chromium Alloys, Master's thesis, Case Western Reserve University, Cleveland, OH 2015.
- [83] Z. S. Basinski, W. Hume-Rothery, and A. L. Sutton, *Proc. R. Soc. London A* **229**, 459 (1955).
- [84] M. Chase, *NIST-JANAF Thermochemical Tables, 4th Edition* (American Institute of Physics, New York, 1998).
- [85] G. Álvarez, A. Zafra, F. Belzunce, and C. Rodríguez, *Theor. Appl. Fract. Mech.* **106**, 102450 (2020).
- [86] A. Trautmann, G. Mori, M. Oberndorfer, S. Bauer, C. Holzer, and C. Dittmann, *Materials* **13**, 3604 (2020).
- [87] A. Atrens, Q. Liu, C. Tapia-Bastidas, E. Gray, B. Irwanto, J. Venezuela, and Q. Liu, *Corros. Mater. Degrad.* **1**, 3 (2020).
- [88] T. Fukuda, *Mater. Trans.* **44**, 1153 (2003).
- [89] N. Buiro, L. Hirsinger, and R. Billardon, *J. Phys. IV (France)* **09**, Pr9-187 (1999).
- [90] E. Tatsumoto and T. Okamoto, *J. Phys. Soc. Jpn.* **14**, 1588 (1959).